

Effects of electronic correlations and disorder on the thermopower of Na_xCoO_2

P. Wissgott, A. Toschi, G. Sangiovanni, and K. Held

Institute for Solid State Physics, Vienna University of Technology, A-1040 Vienna, Austria

(Received 11 April 2011; revised manuscript received 19 May 2011; published 26 August 2011)

For the thermoelectric properties of Na_xCoO_2 , we analyze the effect of local Coulomb interaction and (disordered) potential differences for Co sites with adjacent Na ion or vacancy. The disorder potential alone increases the resistivity and reduces the thermopower, while the Coulomb interaction alone leads only to minor changes compared to the one-particle picture of the local-density approximation. Only combined, these two terms give rise to a substantial increase of the thermopower: the number of (quasi)electrons around the Fermi level is much more suppressed than that of the (quasi) holes. Hence there is a particle-hole imbalance acting in the same direction as a similar imbalance for the group velocities. Together, this interplay results in a large positive thermopower. Introducing a thermoelectric spectral density, we located the energies and momenta regions most relevant for the thermopower and changes thereof.

DOI: [10.1103/PhysRevB.84.085129](https://doi.org/10.1103/PhysRevB.84.085129)

PACS number(s): 71.27.+a, 71.10.Fd

I. INTRODUCTION

The efficient conversion between different forms of energy represents a primary task in technical applications. Thereby the arguably most valuable form is electrical energy. On the other hand, heat energy is widely used in power plants to produce mechanical energy which is then further converted to electricity. The reason for the widespread application of this multiple-step process is based on the lack of an efficient direct alternative.

A direct heat-electricity conversion is possible by the thermoelectric effect or thermopower. The (dimensionless) thermoelectric figure of merit ZT has been established as a benchmark to compare different materials. Values of $ZT \sim 3$ appear to be necessary to trigger an extensive industrial use of thermoelectrics,^{1,2} which could then not only replace traditional methods of energy production but could also increase the efficiency of existing technical implementations such as cars³ or power plants via the conversion of excess heat to electricity.

The development of novel thermoelectric applications follows two routes: First, there is the search for new materials with a large intrinsic ZT which can either be achieved by optimizing features of already known compounds (via, e.g., band-structure engineering⁴) or by the discovery of new classes of materials with peculiar properties (e.g., Kondo systems^{5,6}). Second, one tries to diminish thermal losses due to phonons, i.e. avoiding collective excitations of the crystal by a specific structural arrangement (phonon engineering) such as heterostructuring.^{7,8}

Opposed to other transport properties, as, for example, the electrical conductivity, the magnitude of the thermoelectric effect depends on an asymmetry between the two charge carriers holes and electrons. This asymmetry usually manifests itself in different velocities and/or spectral densities in the vicinity of the chemical potential.

In this paper, we investigate the thermoelectric properties of Na_xCoO_2 taken as a representative compound where the already favorable single-electron features are enhanced by the combination of strong electronic correlations and disorder. We extend the analysis of a previous work⁹ exploring the dependence of the thermopower on various parameters, one at a time as well as combinations of two of them, e.g., disorder and correlation strength at the same time.

As a noninteracting starting point we used the local-density approximation (LDA) result from Ref. 10 fitted to a tight-binding band structure.⁹ Already at the level of LDA the thermoelectric performance of Na_xCoO_2 was found to be high and was understood in terms of the “pudding mold” shape of the decisive a_{1g} band.¹¹ Here, we want to analyze the effects of electronic correlation in this compound and therefore we have combined LDA with dynamical mean-field theory (DMFT).^{12,13} The LDA+DMFT approach is described in Refs. 14–17 and we proceed as in Ref. 18 to compute the thermoelectric response. We focused on the low-energy excitations, which give the main contributions to the thermopower. Earlier LDA+DMFT studies on the spectral properties of Na_xCoO_2 can be found in Refs. 19–22.

In Fig. 1, we show a summary of the main results described in this study: Considering neither disorder nor correlations, the charge-carrier properties are described by the “pudding mold” band, which favors electrons in terms of spectral density, but favors holes with respect to group velocity. The latter effect is larger so that hole transport²⁴ dominates and we get a positive value of the thermopower S (Fig. 1, left panel). Introducing disorder to the system increases the scattering rate of both charge carriers thus diminishing S (Fig. 1, middle panel). If we additionally take into account electronic correlations, the hole spectral density is recovered and can be even overcompensated whereas the number of electrons is further decreased, which overall yields a high thermoelectric response (Fig. 1, right panel). For a more quantitative picture, refer to Fig. 2, where the change of S in the parameter space of correlation U and disorder potential $\Delta\varepsilon$ is visualized. It can be seen that drastic changes happen, for example, for $\Delta\varepsilon = 0.55$ eV where an increasing U leads to an enhancement of S by 200%. Moreover, for even larger values of $\Delta\varepsilon$ and $U = 3.5$ eV we found the maximal values of $S = 80 \mu\text{V}/\text{K}$ in the tested parameter space. Note that the system shows insulating tendency for similar values of $\Delta\varepsilon \gtrsim 0.55$ eV and $U = 0$. This implies that in correlated materials disorder effects may be exploited to enhance the thermopower.

The structure of this paper is as follows: In Sec. I, we introduce the Hamiltonian of the model and describe how standard LDA+DMFT can be expanded by means of coherent

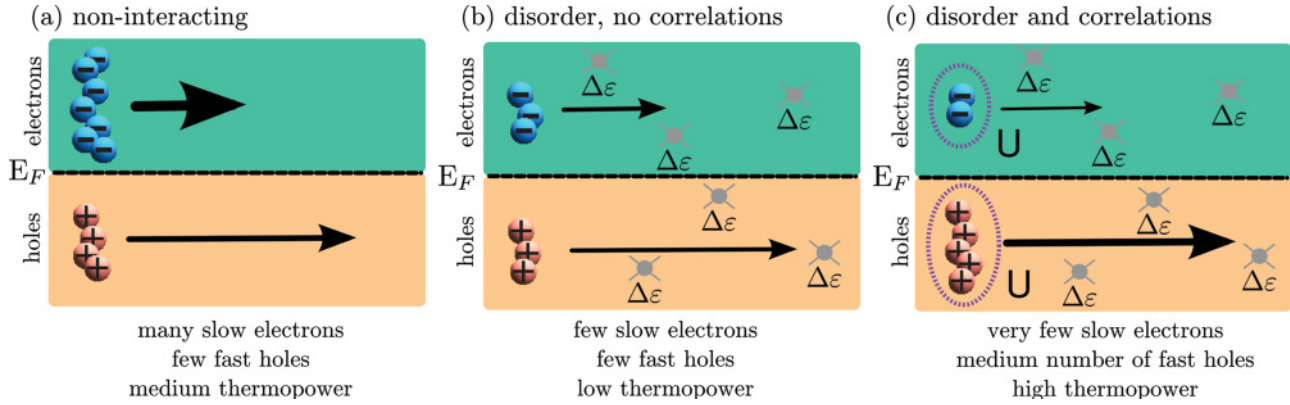


FIG. 1. (Color online) Qualitative effect of disorder and electronic correlations on the charge carriers (Ref. 24) and the thermopower in Na_xCoO_2 . On the vertical axis, energy in arbitrary units is shown with the Fermi level E_F and electrons above and holes below. The horizontal axis schematically indicates the movement through the material with velocities and charge-carrier density according to the length and width of the arrow, respectively. The presence of disorder and electronic correlations is visualized by scattering centers $\Delta\varepsilon$ and the encirclement of the charge carriers accompanied by U , respectively.

potential approximation (CPA) to include disorder. In Sec. II, we depict the linear-response formalism to compute the thermopower S as a functional of spectral density, group velocity, and temperature. Both sections present the necessary details for following our result, which were naturally missing in the short paper Ref. 9

Section III provides an insight to the structural and spectral properties of Na_xCoO_2 missing in Ref. 9. Additionally to the lattice structure, the employed tight-binding approximation is explained in detail. Confirming previous results from Ref. 11, the third-nearest-neighbor hopping appears to play a key role for the transport properties of this triangular compound. Disentangling the spectral contributions and the self-energy from the two nonequivalent lattice sites due to disorder, it is shown that one of the two sites exhibits a much larger correlation effect than the other. A comparison of low-energy spectral properties to experiment concludes this section. In Sec. IV, the main results for the thermopower are presented. The method of visualization of spectral contributions to the thermopower introduced in Ref. 9 is described in detail, as well as new ways to simplify the theoretical thermoelectric analysis.

In an effort to distinguish between the parameters temperature, disorder, and electronic correlation, we investigate their influence on the thermopower with the respective other parameters fixed. It is revealed that the system is very sensitive to small changes of disorder. The impact of correlations on the transport properties is directly connected to the strength of the disorder, which can be seen in a detailed spectral analysis. Towards the end of this section, the dependence of the thermopower on a change of the sodium doping is delineated. Increasing the doping within the investigated doping region appears to increase the thermoelectric effect, which is also supported by experimental results. Finally, we give a conclusion in Sec. V.

II. LDA+DMFT APPROACH INCLUDING CPA

We aim to model Na_xCoO_2 with binary disorder, which corresponds to consider two different sites a, b with an occurrence of $x_a, x_b = 1 - x_a$. In comparison to the standard one-band Hubbard model,²⁵ the disorder Hamiltonian

$$H_{\text{dis}} = - \sum_{ij, \sigma} t_{ij} c_{j\sigma}^+ c_{i\sigma} + U \sum_i n_{i\uparrow} n_{i\downarrow} + \Delta\varepsilon \sum_{i \in b} n_i \quad (1)$$

includes a term contributing only on the site b by a disorder potential $\Delta\varepsilon$. Here, $c_{i\sigma}^+$ and $c_{i\sigma}$ create and annihilate an electron on site i with spin σ , respectively, $n_{i\sigma} := c_{i\sigma}^+ c_{i\sigma}$ is the electron density on site i for the spin σ , U is the local Coulomb interaction.

For disordered systems the coherent potential approximation (CPA)^{26,27} provides a way to treat inequivalent sites in the same spirit as DMFT. In the CPA, the sites a, b are assumed to be surrounded by a self-consistently determined effective medium. Both sites experience the same dynamical mean field, i.e., see the same (averaged) environment given by an impurity Green's function \mathcal{G}_0^{-1} as defined in Ref. 13 or equivalently the same (coherent) potential represented by a self-energy Σ . Even though the mean field \mathcal{G}_0^{-1} is the same, the disorder manifests in two different on-site energies $\varepsilon_a = 0, \varepsilon_b = \Delta\varepsilon$ on the sites a and b , respectively (Fig. 3).

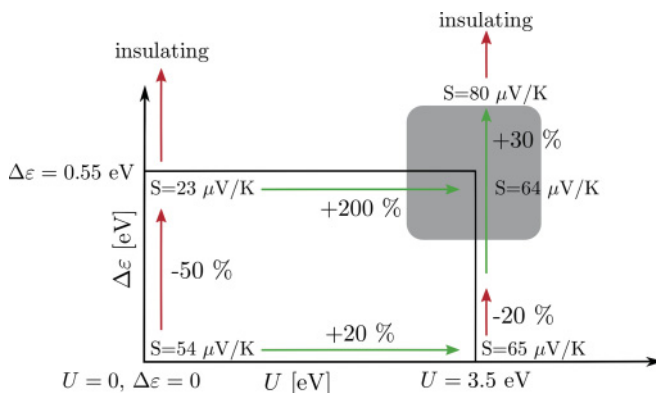


FIG. 2. (Color online) Change of the thermopower S in the parameter space of local Coulomb repulsion U and disorder potential $\Delta\varepsilon$ for $\text{Na}_{0.7}\text{CoO}_2$ at $T = 290$ K. The highlighted regions indicates realistic parameter values for this material.

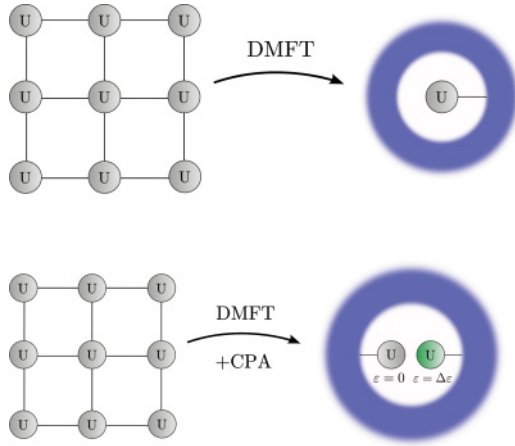


FIG. 3. (Color online) Schematic description of the dynamical mean-field method (DMFT) compared to its combination with the coherent potential approximation (CPA). Top: In standard DMFT the lattice problem is replaced by a site in a self-consistently determined dynamical mean field. Bottom: For the CPA, *two* sites with different on-site potential are connected to the same dynamical mean field.

In DMFT the dynamical mean field \mathcal{G}_0^{-1} determines an action

$$\mathcal{A} := \sum_{\sigma \omega_m} \psi_{\sigma}^{+}(\omega_m) \mathcal{G}_0^{-1}(\omega_m) \psi_{\sigma}(\omega_m) - U \sum_{\sigma} \int_0^{\beta} d\tau' \psi_{\sigma}^{+}(\tau') \psi_{\sigma}(\tau') \psi_{\sigma}^{+}(\tau') \psi_{\sigma}(\tau'), \quad (2)$$

where ψ^{+} , ψ are creation and annihilation operators, respectively, σ is a spin index, β is the inverse temperature, and ω_m are Matsubara frequencies (see, e.g., Ref. 17). The inclusion of (disorder) CPA into DMFT is straightforward (see Fig. 3 for a schematic visualization): Assume for the moment that the effective medium $\mathcal{G}_0^{-1}(i\omega_m)$ is known. Then, the local Green's functions $G_a(r=0, i\omega_m)$, $G_b(r=0, i\omega_m)$ can be determined via the action \mathcal{A} from Eq. (2) by replacing the standard $\mathcal{G}_0^{-1}(\omega_m)$ by $[\mathcal{G}_0^{-1}(\omega_m) - \mathbb{1}_{\varepsilon_{a,b}}]$ with different on-site energies $\varepsilon_a = 0, \varepsilon_b = \Delta\varepsilon$. The local Green's functions G_a, G_b are the local interacting propagators of electrons starting at a, b and returning to the same site a or b , respectively. Then, the total Green's function $G(r=0, i\omega_m)$ is given by the weighted mean

$$G(i\omega_m) = x_a G_a(i\omega_m) + (1 - x_a) G_b(i\omega_m) \quad (3)$$

such that both propagators G_a, G_b are taken into account according to the stoichiometric appearance of the corresponding site x_a or x_b in the lattice.

For the CPA expansion of the DMFT, the effective dynamic medium $\mathcal{G}_0^{-1}(i\omega_m)$ is determined self-consistently. For a given \mathcal{G}_0^{-1} , we obtain the local Green's functions G_a, G_b by two Hirsch-Fye quantum Monte Carlo (HF-QMC) calculations with different on-site potentials $\varepsilon_a = 0, \varepsilon_b = \Delta\varepsilon$. Then, the weighted $G(i\omega_m)$ from Eq. (3) can be used to compute the new self-energy $\Sigma(\omega)$ or equivalently the new effective field \mathcal{G}_0^{-1} via Dyson's equation

$$\Sigma(i\omega_m) = \mathcal{G}_0^{-1}(i\omega_m) - G^{-1}(i\omega_m). \quad (4)$$

With this approach we can include both correlations and disorder in a dynamic mean-field scheme.

III. LINEAR RESPONSE AND DMFT EXPRESSIONS FOR THE THERMOPOWER

In linear response, the thermopower is defined as a ratio of two correlation functions K_1 and K_0

$$S = \frac{k_B}{T} \frac{K_1}{K_0}. \quad (5)$$

Here and throughout, T denotes the temperature. The determination of the correlation functions usually requires a representation of current operators in terms of the electric-field operators ψ^{+}, ψ . The electrical current in imaginary time reads

$$\hat{j}(r, \tau) = \frac{i|e|}{2m} [\psi^{+}(r, \tau) \nabla \psi(r, \tau) - \nabla \psi^{+}(r, \tau) \psi(r, \tau)], \quad (6)$$

which can be found in many textbooks.²⁸ On the contrary, the representation for the heat current has many subtleties and is derived via a continuity equation following Ref. 29,

$$\hat{O}(r, \tau) = -\frac{1}{2m} [\dot{\psi}^{+}(r, \tau) \nabla \psi(r, \tau) + \nabla \psi^{+}(r, \tau) \dot{\psi}(r, \tau)], \quad (7)$$

where the dot denotes a (imaginary) time derivative. Then, the electrical-current-electrical-current correlation function evaluates to (as vertex corrections are absent in single-band DMFT)

$$K_0 = -\frac{2e^2 \pi \hbar}{V} \sum_k |\nabla \varepsilon(k)|^2 \int d\omega A^2(k, \omega) \frac{\partial f(\omega)}{\partial \omega} \quad (8)$$

with V the unit-cell volume, $\hbar \nabla \varepsilon = \partial \varepsilon / \partial k$ the group velocity of the charge carriers, $A(k, \omega)$ the electron spectral function, and $f(\omega)$ the Fermi function. Note that $K_0 = \sigma$ has units of a conductivity ($\text{A V}^{-1} \text{m}^{-1}$). On the other hand, the heat-current–electric-current correlation function reads

$$K_1 = \frac{2|e| \pi c_e \text{eV}}{V} \sum_k |\nabla \varepsilon(k)|^2 \int d\omega A^2(k, \omega) \omega \frac{\partial f(\omega)}{\partial \omega}, \quad (9)$$

where $c_e \text{eV} = 11\,600 \text{ K/eV}$ and K_1 has units ($\text{A J}^{-1} \text{K m}^{-1}$). Combining K_0 and K_1 leads to the thermopower

$$S = -\frac{k_B \beta}{|e|} \frac{\sum_k |\nabla \varepsilon(k)|^2 \int d\omega A^2(k, \omega) \omega \frac{\partial f(\omega)}{\partial \omega}}{\sum_k |\nabla \varepsilon(k)|^2 \int d\omega A^2(k, \omega) \frac{\partial f(\omega)}{\partial \omega}}. \quad (10)$$

Note that this result is expressed in the correct units ($\text{V/K} = \text{J A}^{-1} \text{s}^{-1} \text{K}$) (β times the fraction of K_1 and K_0 remains dimensionless).

For the integral in the denominator of Eq. (10), i.e., K_0 , the contributions with respect to k and ω enter additively, i.e., an asymmetry of $|\nabla \varepsilon(k)|$ with respect to k or $A(k, \omega)$ with respect to (k, ω) is not important. The integral in the numerator of Eq. (10) (K_1) has an additional ω and since $df/d\omega$ is negative, $|\nabla \varepsilon(k)|^2 A^2(k, \omega) \omega df/d\omega$ is positive for $\omega < 0$ (holes) and negative for $\omega > 0$ (electrons).²⁴ Consequently, asymmetry of the group velocity $|\nabla \varepsilon(k)|$ as well as the corresponding asymmetry of the spectrum $A(k, \omega)$ are decisive for a high thermopower.³⁰ In our model material $\text{Na}_x \text{CoO}_2$ this is accomplished by a low group velocity $\nabla \varepsilon(k)$ for electrons, whereas holes move much faster through the system. For the

band structure this means we have a flat region directly above $\omega > 0$ the Fermi level at $\omega = 0$ and a steep slope directly below $\omega < 0$. This is the feature usually denoted by “pudding mold” (cf. Ref. 11).

From Eq. (8) it becomes clear that K_0 is always positive, since $\partial f/\partial\omega$ is negative for all ω and the other quantities only enter quadratically. At the same time K_1 may be either positive or negative depending on whether the hole contribution $\omega < 0$ or electron contribution $\omega > 0$ dominate. This reflects obviously in the sign of the thermopower S .

IV. STRUCTURE AND SPECTRAL PROPERTIES OF SODIUM COBALTATE

In 1997, Terasaki and co-workers³¹ identified NaCo_2O_4 ($\hat{=} \text{Na}_{0.5}\text{CoO}_2$) as a promising candidate for thermoelectric applications. Other publications confirmed the results of a positive thermopower of the order of $100 \mu\text{V}/\text{K}$ even for other sodium contents.^{32–34} With the appearance of superconductivity in the H_2O intercalated compounds,^{35,36} the material Na_xCoO_2 once again proved to exhibit surprising features.

Recently, Kuroki *et al.*¹¹ argued in favor of band-structure properties playing the most important role in determining the thermopower in Na_xCoO_2 . In their study, Kuroki and co-workers used Boltzmann’s equation to compute the Seebeck coefficient $S(T)$. Here, we go beyond that approach and propose an method to compute S by means of linear-response theory including correlations by DMFT and disorder by CPA (cf. Secs. II and I, respectively). As representative compound, we choose a doping of $x_{\text{Na}} = 0.7$, i.e., $\text{Na}_{0.7}\text{CoO}_2$.

A. Lattice structure

In Fig. 4, we plot the crystal structure of the system. Sodium cobaltate NaCoO_2 consists of alternating layers of sodium and cobaltate CoO_2 . The Co atoms are arranged in a trigonal lattice structure with a nearest-neighbor distance of 2.84 \AA ; see Ref. 37. Each cobalt atom is surrounded by six oxygen atoms in form of a tilted octahedron. The Na atoms are located in their own layer halfway between the CoO_2 layers.

The exact lateral position of the sodium atoms within their layer and mutual shifts of the CoO_2 layers depend nontrivially on doping, temperature, etc. For example, Huang *et al.*³⁸ report a change of the Na positions for $x_{\text{Na}} = 0.75$ around $T = 320 \text{ K}$. On the other hand, an earlier work of Yakabe *et al.*³⁴ find three typical phases of Na_xCoO_2 as x_{Na} changes from 0.55 to 1. Since almost all of the transport takes place in the CoO_2 layers, mutual shifts of the cobaltate layers only weakly influence the thermopower results. We therefore assume the CoO_2 layers to be all equivalent, i.e., there is no structural shift.

The lateral position of Na in the compound, on the other hand, is a delicate topic. Many Na coordinates have been reported, mainly the position directly above the Co atom ($x = 0, y = 0$) and a position which is aligned to the O atoms ($x = 2/3, y = 1/3$).^{10,37} Moreover, the former reference also suggests movement of the sodium ions. For lower temperatures Zandbergen³⁹ found two different types of Co atoms, namely Co^{3+} and Co^{4+} . We therefore assume that the cobaltate system shows binary disorder, even if the sodium atoms are distributed on multiple sites. As we are interested in

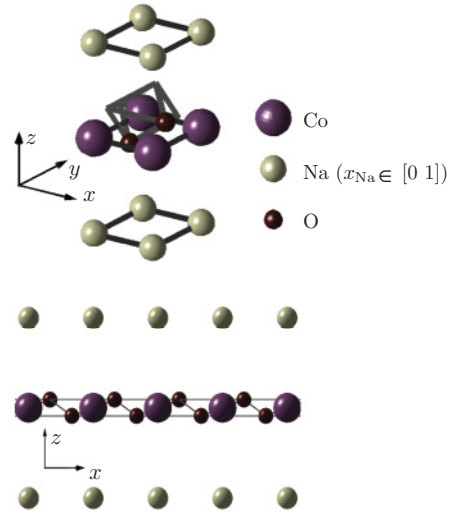


FIG. 4. (Color online) Top: Unit cell of NaCoO_2 according to the crystal structure from Ref. 37. We additionally visualize the Co and Na bondings as well as one distorted O octahedron. The actual size of the atoms is different from the hard spheres and the distance between the Co and Na layers is larger than shown. For the $\text{Na}_{0.7}\text{CoO}_2$ system, we assume that only 70% of the Na position are occupied. Bottom: Cobalt layers and the distorted oxygen octahedra.

relatively high temperatures for thermoelectric applications, a possible ordering of the Na ions does not appear to be relevant.⁴⁰ For simplicity, we assume the Na to be located on the $(x = 0, y = 0, z = 1/2)$ site directly above the cobalt. Thus we can still assign a Na atom to one specific Co site. This corresponds to the same “virtual crystal approximation,” which has been used for the underlying band-structure calculation.¹⁰

For a doping of $x_{\text{Na}} = 0.7$, 70% of the sodium sites are actually occupied and we consequently have 30% vacancies in the sodium layers. The hereby inequivalent Co sites in the cobaltate layers are denoted by Co_{Na} ($\hat{=} \text{Co}^{+3}$) and Co_{vac} ($\hat{=} \text{Co}^{+4}$) depending on whether or not they have a close sodium atom. As we will show below, electrons of one band with weak k_z dispersion are responsible for transport. We denote the filling of this band at the two different sites by n_{Na} and n_{vac} , respectively. Due to the disorder, these electrons tend to be at cobalt sites Co_{Na} with a sodium partner, by means of simple electrostatic attraction to the Na^+ ionic cores. The strength of this tendency is governed by the disorder potential $\Delta\varepsilon$, i.e., the difference of the on-site potential of the two nonequivalent sites. Additionally, many-body effects can influence the movement of electrons and holes in the disordered crystal.

To determine the relevant energy bands in this material, it is vital to understand the crystal-field splitting of the NaCoO_2 lattice. In this light, as part of a thought experiment, the gradual transition between the Co atomic orbitals and their bulk material analogs can be useful: The five atomic d orbitals can be classified according to their radial and spatial dependence of the corresponding wave functions. In a Cartesian coordinate system one has three planar orbitals $|xy\rangle$, $|yz\rangle$, $|zx\rangle$ denoted by t_{2g} and two orbitals $|3z^2 - r^2\rangle$, $|x^2 - y^2\rangle$ denoted by e_g . Refer to Fig. 5 for a visualization of these states. The electron

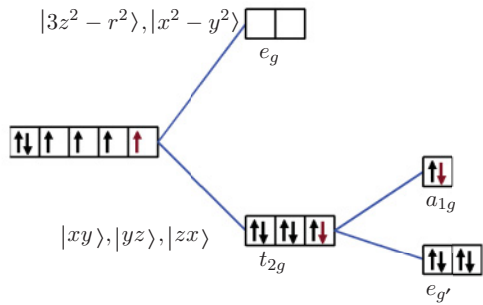


FIG. 5. (Color online) The breakup of the degeneracy of the d orbitals: First, the five d basis energetically split up in three t_{2g} orbitals and two e_g orbitals in an octahedral configuration. Second, the three t_{2g} split up in one a_{1g} and two $e_{g'}$ due to the distortion of the oxygen octahedra. The energy differences shown in this plot are symbolic. We also visualize the occupancy of the orbitals in the different situations, where oxidation state of the cobalt atom in the compound is Co^{+3} (Co^{+4}) if a Na partner is (not) present. This additional electron whose presence depends on a sodium donor is shown as an arrow with different color.

configuration of single-atom cobalt is $[\text{Ar}]3d^74s^2$. According to Hund's rule, the d electrons try to occupy all the orbitals and maximize the total spin (in this case $S = 1$), if the d orbitals are degenerate.

Atomic orbitals hybridize if the atom is placed in bulk material. However, one can use the picture of atomic orbitals as a starting point to gradually include the influence of the crystal structure. In CoO_2 , the Co atom is surrounded by an octahedron of six O atoms. The e_g orbitals of Co have a large part of their spatial probability density close to these ligands. Since the O ion is negatively charged, the e_g orbitals pointing toward the oxygen become less favorable for electrons to occupy than in the atomic case.

Moreover, the O octahedra that surround the Co atom are distorted; cf. Fig. 4. One can show that this does not lift the degeneracy of the e_g , but, on the other hand, the t_{2g} states split up in one a_{1g} and two energetically lower $e_{g'}$ orbitals. These a_{1g} and $e_{g'}$ states do not correspond any longer to single t_{2g} orbitals, but are rather linear combinations thereof. These considerations lead to the orbital structure visualized in Fig. 5.

When we go beyond a single Co site, the picture of local orbitals is not fully valid any more, but is rather replaced by bands representing a certain dispersion relation. Still, we can look for bands in the band structure that have predominant a_{1g} , $e_{g'}$, or e_g orbital character and which arrange in the same energetic order as the orbitals in Fig. 5.

The band structure from Singh¹⁰ provided the starting point for the tight-binding approximation. To mimic disorder at the level of LDA, Singh used a NaCo_2O_4 supercell with twice as many bands due to the doubling of the unit cell. Following a different approach, we extract an approximation for one single a_{1g} band of NaCoO_2 from the LDA result¹⁰ and include the disorder in a second step at the level of the DMFT algorithm; cf. Sec. I.

Corresponding to atomic valence orbitals, one also finds valence bands within a solid-state compound. Analogously,

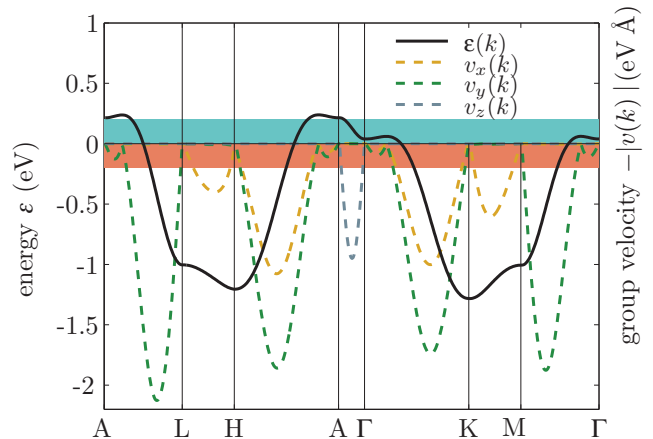


FIG. 6. (Color online) Tight-binding approximation (solid line) and group velocities (dashed lines) for $\text{Na}_{0.7}\text{CoO}_2$.

very tightly bound “core bands” and, in the ground state unoccupied “conductance bands” may be identified. In cobaltate, the valence bands are the three oxygen p orbitals and the three cobalt d - t_{2g} orbitals. Due to high electronegativity, the p bands of O are well below the Co bands. On the other hand, the sodium s orbitals belong to the conduction bands and are even above the unoccupied Co e_g bands. The number of bands considered in the LDA+DMFT model strongly influences the computational effort necessary to solve it. Whereas the decrease to the complexity for the tight-binding approximation is not decisive, the effort for the DMFT calculations heavily depends on the number of bands. We aim therefore to minimize the number of orbitals, without losing (too much) physically relevant information.

The oxidation state of Co in the compound is +3 in NaCoO_2 and +4 in CoO_2 , respectively. Thus of the nine valence electrons 6 and 5, respectively, actually fill the cobalt d bands. For transport properties a rather small energy interval of the order of $\mathcal{O}(k_B T)$ around the Fermi edge is important, since electrons in this regime can be thermally activated. Only the t_{2g} bands are located within that interval (under normal conditions). In the following, we will assume that the hybridization of $e_{g'}$ and a_{1g} bands is negligible. With this assumption, the crystal-field splitting visualized in Fig. 5 guarantees that the $e_{g'}$ orbitals remain filled and that, for transport calculations, restricting to the partly occupied a_{1g} orbital is sufficient.

To extract the two effective a_{1g} bands from the band structure of NaCo_2O_4 , Kuroki and Usui made a tight-binding fit,⁹ which is shown in Fig. 6. Since we aim to include only one a_{1g} band in the DMFT, we have to find the corresponding single tight-binding band for NaCoO_2 . Though NaCoO_2 is similar to NaCo_2O_4 , there are subtle differences: Since the supercell for NaCo_2O_4 contains two Co atoms the corresponding Brillouin zone has half the size of the one for NaCoO_2 in the z direction. Thus the single a_{1g} band will not match exactly one of the two bands for NaCo_2O_4 of the original fit. The lower band of the two highlighted bands mainly belongs to the cobalt site in NaCo_2O_4 with a sodium partner. As an approximation, we therefore take the tight-binding parameters for this band, but use the (larger) Brillouin zone of NaCoO_2 in DMFT. The final

TABLE I. Tight-binding parameters obtained by a parameter fit to LDA data.

Notation	Intra/interlayer	NN	Values (par. fit)
t_1	intralayer	1st	0.1800
t_2	intralayer	2nd	-0.0388
t_3	intralayer	3rd	-0.0270
t_4	intralayer	4th	0.0004
$t_{z,0}$	interlayer		-0.0180
$t_{z,1}$	interlayer	1st	-0.0049
$t_{z,2}$	interlayer	2st	-0.0016
$t_{z,3}$	interlayer	3rd	0.0011
$t_{z,4}$	interlayer	4th	0.0005

a_{1g} band is shown in Fig. 6 together with the corresponding group velocities $\nabla \varepsilon^{\text{TB}}(k) = \{\vec{v}_x, \vec{v}_y, \vec{v}_z\}$.

In the following, we discuss the applied tight-binding approximation: Let the a_{1g} band have the dispersion relation $\varepsilon^{\text{LDA}}(k)$ given by the data points that are the output of the LDA calculation. We now aim to replace $\varepsilon^{\text{LDA}}(k)$ by an analytic expression, which then can be easily used to obtain the group velocity $\nabla \varepsilon^{\text{LDA}}(k)$. To this end, we make a tight-binding ansatz with nine parameters,

$$\varepsilon^{\text{LDA}}(k) \approx \varepsilon^{\text{TB}}(k) = \sum_{n=1}^9 t_n \sum_{j=1}^{\#NN} e^{ik \cdot r_{jn}}, \quad (11)$$

where $\#NN$ denotes the number of nearest neighbors of n th order and r_{jn} enumerates the corresponding n th nearest-neighbor position. Due to inversion symmetry the exponential function in Eq. (11) can be simplified as

$$\varepsilon^{\text{LDA}}(k) \approx \varepsilon^{\text{TB}}(k) = 2 \sum_{n=1}^9 t_n \sum_{j=1}^{\#\overline{NN}} \cos(k \cdot r_{jn}). \quad (12)$$

Here, $\#\overline{NN}$ means that the pairs of atoms connected by inversion symmetry are counted only once. The first four parameters t_1, \dots, t_4 describe the hopping between nearest neighbors within one Co plane. The fifth parameter t_{z0} measures the probability of Co-interplane hopping from a cobalt atom to another cobalt directly above (below). The final four parameters t_{z1}, \dots, t_{z4} describe processes of combined interplane and nearest-neighbor hopping.

The fitted set of parameters⁹ are listed in Table I. The final tight-binding fit of the a_{1g} band yields a bandwidth of 1.5 eV and is, as expected, predominately dispersive in the x - y plane (corresponding to the cobaltate layers).

With the analytic dispersion $\varepsilon^{\text{TB}}(k)$ from Eq. (12), we may investigate which tight-binding parameters are necessary for the characteristics of the noninteracting LDA density of states,

$$N(\omega) := -\frac{1}{\pi} \text{Im} \left[\sum_k \frac{1}{\omega - \varepsilon^{\text{TB}}(k) + i\delta} \right], \quad (13)$$

with $\delta \rightarrow 0^+$. The functions $N(\omega)$ considering hopping up to 1, \dots , 9 nearest neighbors are plotted in Fig. 7 (the final solid line corresponds to the LDA DOS). Consistent with the results from Kuroki,¹¹ we observe that hopping up to the third-nearest neighbor is necessary to obtain the important

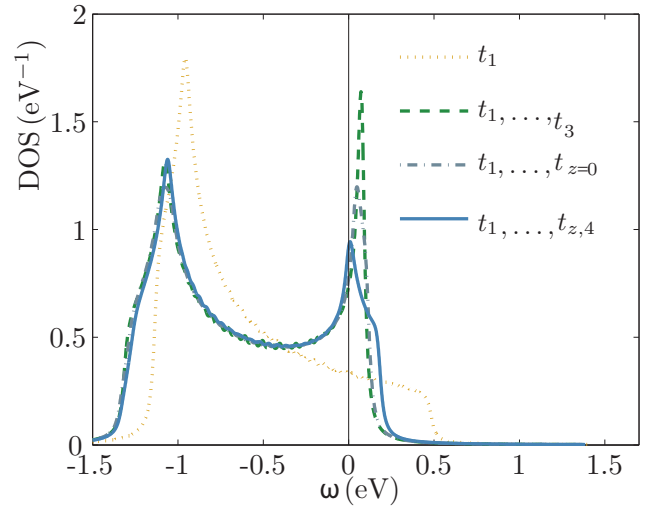


FIG. 7. (Color online) Density of states (DOS) $N(\omega)$ considering an increasing number of neighbors in the tight-binding approximation using the parameters from Table I. The dotted line corresponds to the DOS computed only with nearest-neighbor hopping, whereas the solid curve is computed with all nine parameters. A decisive hopping appears to be the one to the third-nearest neighbor, where a significant change of the characteristics of the DOS can be observed.

upper van Hove-like peak, which will play a role for the explanation of the large thermopower below. If we also consider interplane hopping (i.e., $t_{z,i} \neq 0$) the peak above $\omega = 0$ is less pronounced. Leaving the $2d$ regime this is the standard behavior for van Hove peaks, which are usually damped in $3d$ with respect to lower dimensions. The final DOS is dominated by two major peaks, which are approximately 1 eV apart.

B. LDA+DMFT self-energy and spectrum of $\text{Na}_{0.7}\text{CoO}_2$

With the tight-binding dispersion relation ε^{TB} , we now run the DMFT algorithm depicted in Sec. I. For given temperature T , correlation U , doping x_{Na} , and disorder potential $\Delta\varepsilon$, we obtain the self-energy $\Sigma(i\omega_m)$ at the Matsubara frequencies $\omega_m = (2m + 1)\pi/\beta$, and the Green's function $G(\tau)$. Here, and throughout this work, β denotes the inverse temperature in eV^{-1} defined by $\beta := 11600/T \text{ eV}^{-1}$. From the imaginary part of the self-energy $\text{Im}\Sigma(i\omega)$ we can extract information about the strength of correlation and disorder effects in the system. For example, a divergent

$$\lim_{\omega \rightarrow 0^+} \text{Im}\Sigma(i\omega) = \pm\infty \quad (14)$$

indicates that the charge carriers are localized, which leads to an insulating phase. On the other hand, a correlated metal usually yields

$$\lim_{\omega \rightarrow 0^+} \text{Im}\Sigma(i\omega) = 0, \quad (15)$$

with a quasiparticle weight $Z \neq 1$.

In Fig. 8 (bottom), we plot the self-energy $\text{Im}\Sigma$ over the Matsubara frequencies ω_m for our set of initial parameters,

$$\{T = 290 \text{ K}, U = 3.5 \text{ eV}, x_{\text{Na}} = 0.7, \Delta\varepsilon = 0.55 \text{ eV}\}. \quad (16)$$

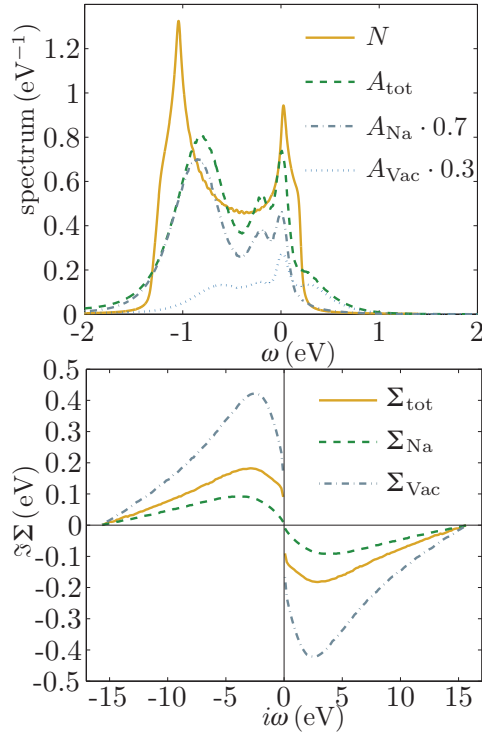


FIG. 8. (Color online) Top: k -integrated spectra $A(\omega)$ obtained by DMFT and maximum entropy method compared to the noninteracting DOS $N(\omega)$. Bottom: Self-energy $\text{Im}\Sigma(i\omega)$ on the imaginary axis. Note that sodium and vacancy contributions are resolved.

Note that here we employ similar parameters as in a previous LDA+DMFT calculation for $\text{Na}_{0.7}\text{CoO}_2$,²³ which did not, however, analyze transport properties.⁴¹ At first glance, the overall $\text{Im}\Sigma_{\text{tot}}$ shows characteristics of a bad metal,⁴² since in the whole temperature range considered it neither diverges nor converges to 0 for $\omega \rightarrow 0$. Hence the separation of correlation and disorder effects on $\text{Im}\Sigma$ needs further investigation. As a first step, we can also visualize the contributions of the two sites Co_{Na} and Co_{Vac} to the self-energy $\text{Im}\Sigma_{\text{tot}}$. Following Sec. I, these contributions are computed via Dyson's equation with the corresponding Green's function, i.e.,

$$\Sigma_{\text{Na}} = \mathcal{G}_0^{-1} + \Delta\varepsilon - G_{\text{Na}}^{-1}, \quad (17)$$

$$\Sigma_{\text{Vac}} = \mathcal{G}_0^{-1} - G_{\text{Vac}}^{-1}, \quad (18)$$

$$\Sigma_{\text{tot}} = \mathcal{G}_0^{-1} - G^{-1}, \quad (19)$$

where $G = x_{\text{Na}}G_{\text{Na}} + x_{\text{Vac}}G_{\text{Vac}}$. We observe that the self-energy $\text{Im}\Sigma_{\text{Na}}$ for the sites Co_{Na} is metallic, the other contribution $\text{Im}\Sigma_{\text{Vac}}$ for Co_{Na} showing insulating tendency.

Equivalent to the self-energy $\text{Im}\Sigma(i\omega)$ connected to the influence of correlation *and* disorder, the Green's function $G(\tau)$ provides information about the many-body excitations of the system, as the k -integrated spectrum $A(\omega)$ is given implicitly by

$$G(\tau) = \int d\omega \frac{e^{\tau(\mu-\omega)}}{1 + e^{\beta(\mu-\omega)}} A(\omega).$$

To calculate the spectral functions, we employ the maximum entropy method (see, for example, Refs. 43 and 44). In Fig. 8 (top), we plot the total spectrum $A_{\text{tot}}(\omega)$ for the a_{1g} band and

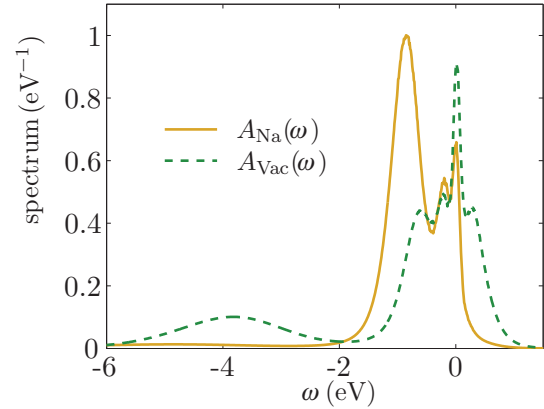


FIG. 9. (Color online) The two contributions $A_{\text{Na}}(\omega)$ and $A_{\text{Vac}}(\omega)$ to the overall spectrum $A_{\text{tot}}(\omega)$ *without* the stoichiometric weighting factor. The filling at the sites Co_{Na} is $n_{\text{Na}} = 0.91$, therefore correlation effects are negligible. For Co_{Vac} with $n_{\text{Vac}} = 0.71$, on the other hand, the formation of a quasiparticle peak at the Fermi edge $\omega = 0$, a lower Hubbard band at $\omega \approx -U = -3.5$ eV, and an upper Hubbard band at $\omega \approx 0.5$ eV can be observed. The center of the two spectra are approximately shifted by the disorder potential $\Delta\varepsilon = 0.55$ eV with respect to each other.

compare it to the contribution of the two sites $\text{Co}_{\text{Na}}, \text{Co}_{\text{Vac}}$ as well as to the noninteracting density of states (DOS) $N(\omega)$. Note that we do not show here the lower Hubbard band at $\omega \approx -U = -3.5$ eV. At first glance, the changes between the $N(\omega)$ to $A_{\text{tot}}(\omega)$ are not significant. But since two contributions $A_{\text{Na}}, A_{\text{Vac}}$ with two different electron fillings

$$\begin{aligned} n_{\text{Na}} &= 2 \times 0.91, \\ n_{\text{Vac}} &= 2 \times 0.71 \quad (n_{\text{tot}} = 2 \times 0.85 = 1 + x_{\text{Na}}) \end{aligned} \quad (20)$$

mix, a separate investigation of the two spectra is useful (note that $n_{\text{Na}}x_{\text{Na}} + n_{\text{Vac}}x_{\text{Vac}} = n_{\text{tot}}$). On Co_{Na} sites, the a_{1g} band is almost filled, whereas on Co_{Vac} the value is closer to half filling, where correlation effects are expected to be stronger. In fact, as can be seen in Fig. 9, the formation of a quasiparticle peak at $\omega = 0$ and a lower Hubbard band at $\omega \approx -U = -3.5$ eV in the spectrum A_{Vac} for the sites Co_{Vac} can be observed. Especially the Fermi-liquid behavior for small ω may be a decisive ingredient for higher thermopower, since the spectral weight in the thermally activated energy interval is crucial, as already discussed in Sec. II. This analysis indicates that disorder enhances the effect of correlations in the compound driving the sites Co with Na vacancy, closer to half filling. As a consequence, the quasiparticle peak for a given correlation U is more pronounced than in the case without disorder.

Analogously to the filling, one can also investigate the approximate renormalization of the two bands

$$Z_{\text{Na}} = 0.88, Z_{\text{Vac}} = 0.36 \quad (Z_{\text{tot}} = 0.48), \quad (21)$$

which was obtained from $\text{Im}\Sigma(i\omega_m)$ by using the tangent of the two Matsubara frequencies closest to the origin. These values should be considered with caution, since the disorder perturbs the Fermi-liquid behavior at both sites Co_{Na} and Co_{Vac} . However, as Fig. 9 indicates, $\text{Na}_{0.7}\text{CoO}_2$ can be interpreted as a system consisting of sites with large correlations Co_{Vac} , and sites Co_{Na} where correlation effects are weak.

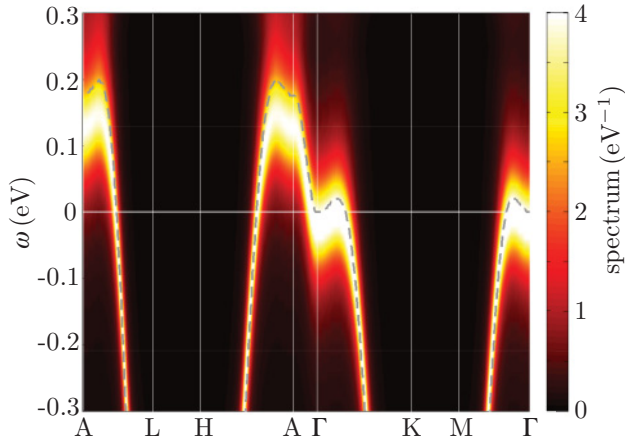


FIG. 10. (Color online) Spectral function $A(k, \omega)$ for $T = 290$ K obtained by a Taylor fit of the DMFT self-energy. The color code of the values of $A(k, \omega)$ is given by the color bar on the right-hand side. The dashed line corresponds to the noninteracting tight-binding dispersion relation.

Apart from the k -integrated spectrum $A(\omega)$, we are also interested in the k -resolved quantity $A(k, \omega)$, which is inserted in Kubo's formula (10). Therefore we need an analytic continuation $\Sigma(i\omega) \rightarrow \Sigma(\omega)$, which is, in general, nontrivial. The behavior of $\Sigma(\omega)$ further away from the Fermi level is not important for transport properties and a Taylor fit is hence sufficient. With the self-energy $\Sigma(\omega)$ the spectrum is calculated as

$$A(k, \omega) = -\frac{1}{\pi} \frac{\text{Im}[\Sigma(\omega)]}{\{\omega + \mu - \varepsilon(k) - \text{Re}[\Sigma(\omega)]\}^2 + \{[\text{Im}\Sigma(\omega)]\}^2}, \quad (22)$$

where μ is the chemical potential from the DMFT calculation. A visualization of the approximation for $A(k, \omega)$ compared to the tight-binding band can be found in Fig. 10.

Let us remark here that it cannot be expected that the electronic structure or spectra match the experimental results in a large energy interval around $\omega = 0$ for a model without the e_g' bands. However, angle-resolved photoemission spectroscopy (ARPES) data from Yang *et al.*⁴⁵ indicate that the e_g' bands, which appear to cross the Fermi edge in LDA, actually do not contribute to the Fermi surface, i.e., are shifted down in energy by many-body effects. Thus a comparison to experimental data may well be accurate in the vicinity of the Fermi level.

In Fig. 11, we show the numerically obtained spectra and the corresponding ARPES data.⁴⁵ For a direct comparison, all numerical results are already multiplied with the Fermi function $f(\omega, \beta) = (e^{\beta\omega+1})^{-1}$ with $T = 290$ K as in the experiment (we thus assume that the spectra do not change qualitatively as $T_{\text{num}} = 290$ K \rightarrow $T_{\text{exp}} = 40$ K). On the left-hand side the k -resolved spectrum $A(k, \omega)$ is plotted for various values of k along the k path $\Gamma \rightarrow K$. In the inset, we give the corresponding experimental results. The reason for the good agreement is the large a_{1g} character of the experimental spectra. On the right-hand side of Fig. 11, we compare the k -

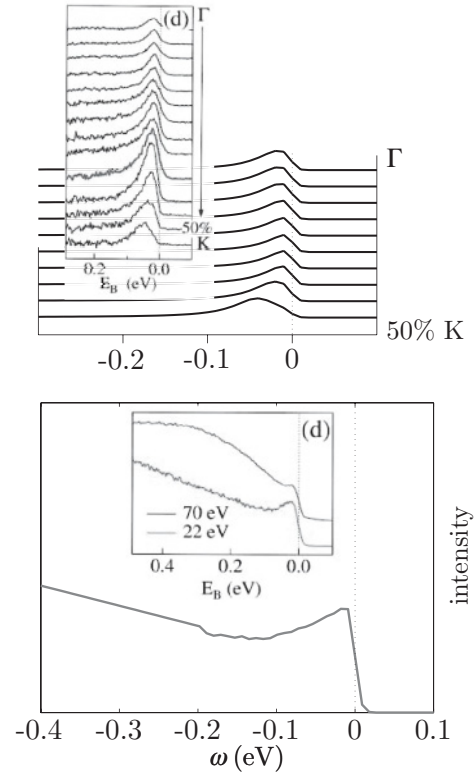


FIG. 11. (Color online) Top: Comparison of the spectrum $A(k, \omega)$ to ARPES results (inset taken from Ref. 45). In experiment, the peaks correspond to a_{1g} excitations. Bottom: k -integrated spectrum $A(\omega)$ and corresponding experimental results (inset taken from Ref. 45). The two slopes in the inset are spectra for different photon energies. For comparison, a linear background signal for $\omega < -0.2$ eV has been added by hand to the numerical results.

integrated spectrum $A(\omega)$. To simulate the e_g' background we add a linear function for $\omega < 0.2$ eV. Again the data coincide qualitatively, as the inset with the experimental results shows.

V. THERMOPOWER

In order to understand the influence of temperature, disorder, correlations, and doping on the self-energy and the thermopower, in this section we will investigate their effect separately with the other parameters kept fixed. For disorder and correlations, however, it is revealed that their effect strongly depends on the respective other parameter. We therefore discuss combined effects of disorder and correlations in its own subsection. Before starting with the first parameter, let us introduce some helpful quantities that will be helpful in the analysis. In Sec. II, we derived the expression $S(T) \sim K_1/K_0$ for the thermopower. The pivotal quantity, which we now focus on, is K_1 depicted in Eq. (9) and therein especially the kernel as a function of (k, ω) . In most of the cases, changes of K_1 directly reflect in the thermopower S . If we separate the factors in the kernel for the initial parameters (16), we arrive at contributions visualized in Fig. 12. Investigating these contributions can lead to a deeper understanding of the important processes in thermoelectric transport. In order to factorize the total kernel \mathcal{K}_{tot} , we define five auxiliary functions

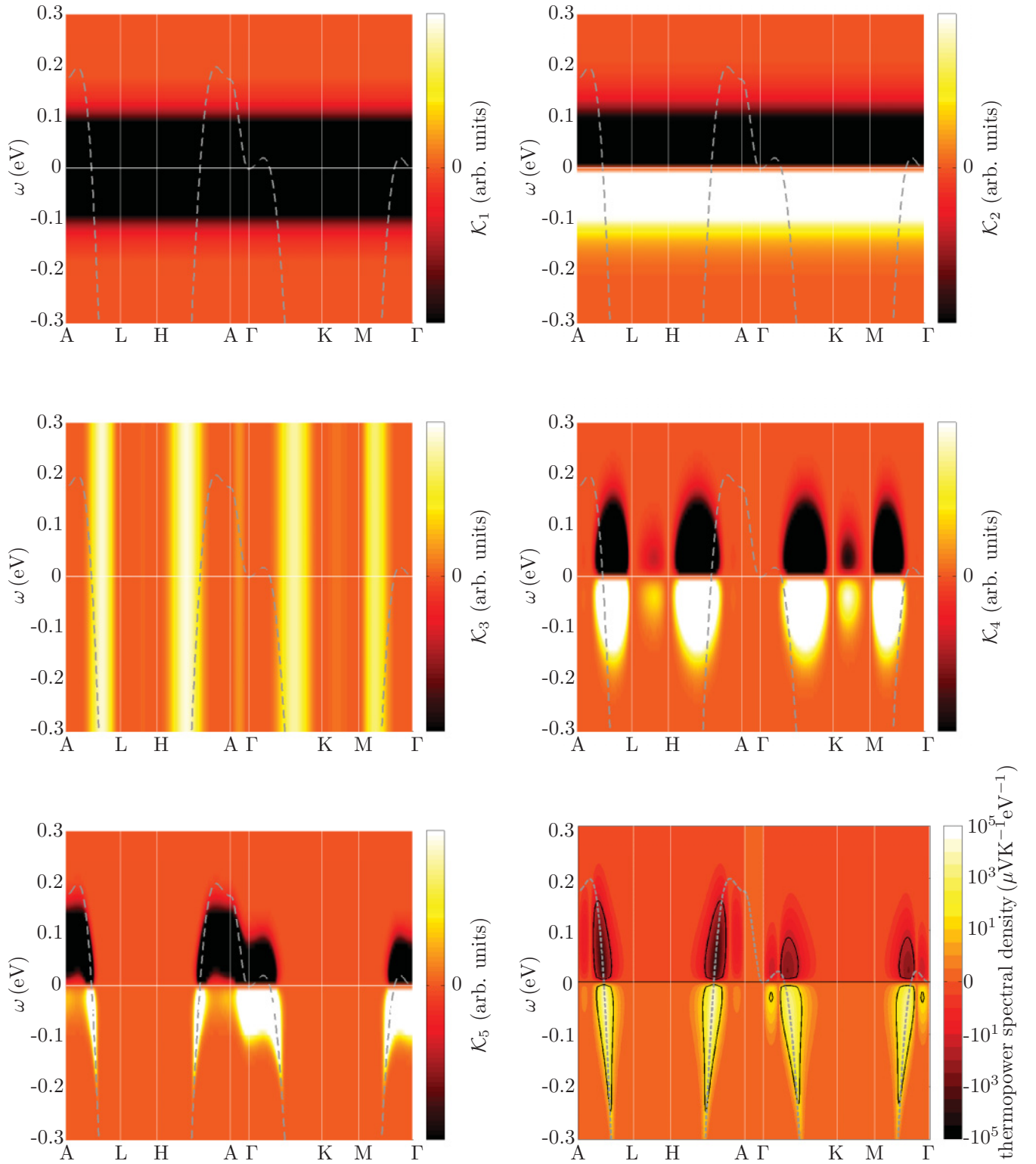


FIG. 12. (Color online) Contributions $\mathcal{K}_1, \dots, \mathcal{K}_5, \mathcal{K}_{\text{tot}}$ to the thermopower S for $T = 290$ K according to Eqs. (23)–(28). Positive values are emphasized by bright (yellow) domains, negative contributions are visualized by dark (red) domains. The units of the kernels $\mathcal{K}_1, \dots, \mathcal{K}_5$ are arbitrary, but domains with brighter or darker scale (more intense red or blue colors) correspond to larger positive or negative values, respectively. As a dashed line, we also plot the LDA band structure. The solid line shows the isovalues $\pm 10^2 \mu\text{V K}^{-1} \text{eV}^{-1}$ for the thermopower spectral density.

of k and ω ,

$$\mathcal{K}_1(k, \omega) := \frac{\partial f(\omega, T)}{\partial \omega}, \quad (23)$$

$$\mathcal{K}_2(k, \omega) := \frac{\partial f(\omega, T)}{\partial \omega} \omega, \quad (24)$$

$$\mathcal{K}_3(k, \omega) := |\nabla \varepsilon(k)|^2, \quad (25)$$

$$\mathcal{K}_4(k, \omega) := |\nabla \varepsilon(k)|^2 \frac{\partial f(\omega, T)}{\partial \omega} \omega, \quad (26)$$

$$\mathcal{K}_5(k, \omega) := A^2(k, \omega) \frac{\partial f(\omega, T)}{\partial \omega} \omega, \quad (27)$$

$$\mathcal{K}_{\text{tot}}(k, \omega) := \frac{k_B}{T} \frac{2\pi e}{K_0} |\nabla \varepsilon(k)|^2 A^2(k, \omega) \frac{\partial f(\omega, T)}{\partial \omega} \omega, \quad (28)$$

where we included all prefactors in \mathcal{K}_{tot} such that $S = \sum_k \int d\omega \mathcal{K}_{\text{tot}}(k, \omega)$. The total kernel \mathcal{K}_{tot} may thus be interpreted as a ‘‘thermopower spectral density’’ determining the contribution to S in (k, ω) space. In the following we restrict ourselves to in-plane transport, i.e., we set $|\nabla \varepsilon(k)|^2 = \vec{v}^2 = \vec{v}_x^2 + \vec{v}_y^2$.

In Fig. 12, a visualization of $\mathcal{K}_1, \dots, \mathcal{K}_5, \mathcal{K}_{\text{tot}}$ for $\{T = 290 \text{ K}, U = 3.5 \text{ eV}, \Delta \varepsilon = 0.55 \text{ eV}\}$ is shown. The derivative of the Fermi function \mathcal{K}_1 constitutes an energy interval around the Fermi edge, where electrons are thermally activated. Electronic transport outside of this interval is exponentially suppressed. The different sign of the charge carriers electrons (negative) and holes (positive) is accounted for by the factor ω in \mathcal{K}_2 . Thus Fig. 12 (top right) shows the charge carriers activated for transport with respect to sign. On the other hand, the group velocity \mathcal{K}_3 is a quantity that only depends on the band structure. As a consequence, \mathcal{K}_3 will be large whenever the slope of $\nabla \varepsilon(k)$ is steep; cf. Fig. 12 (middle left). Combining the latter three contributions leads to \mathcal{K}_4 , shown in Fig. 12 (middle right). We observe that the values are still distributed symmetrically with respect to the Fermi level. The effect of the temperature and spectrum without the group velocity is encoded in \mathcal{K}_5 . There appear to be more contributions from the electrons $\omega > 0$ [Fig. 12 (bottom left)]. Finally, the thermopower spectral density \mathcal{K}_{tot} indicates the regions of (k, ω) space that contribute to the thermopower; cf. Fig. 12 (bottom right). The function \mathcal{K}_{tot} yields both positive (holes) and negative (electrons) contributions to the thermopower, which may in principle also annihilate each other. In fact, that is the usual behavior for most materials where the thermopower S is therefore only of the order of $\pm \mathcal{O}(1) \mu\text{V}/\text{K}$. In our example, the electron contributions are significantly smaller than hole contributions, and this imbalance reflects itself on a positive thermopower S .

A. Effects of the temperature

Before considering the numerical results of the model system $\text{Na}_{0.7}\text{CoO}_2$, we discuss the effects of temperature to the thermopower S by a rather general approach analyzing the thermal dependence of the kernel $\mathcal{K}_5(k, \omega)$. Let us assume for the moment the extreme case that the spectrum $A(k, \omega) \approx A(k)\Theta(-\omega)$, i.e., only holes contribute to the thermopower. Then, we can solve the integral

$$I(\beta) := \int_{-\infty}^0 d\omega \frac{\partial f(\omega, \beta)}{\partial \omega} \omega \quad (29)$$

to obtain an approximation of the thermal dependence of the thermopower S :

$$\begin{aligned} I(\beta) &= f(\omega, \beta) \omega \Big|_{-\infty}^0 - \int_{-\infty}^0 d\omega f(\omega, \beta) \\ &= \frac{\ln(2)}{11\,600} T [\text{eV}]. \end{aligned}$$

Analogous considerations for the conductivity $\sigma = K_0$ yield a factor β , which cancels with β from the definition of $S = k_B \beta e^{-1} K_1 K_0^{-1}$. Thus a linear dependence $S \propto T$ represents a first approximation for the thermopower. Since extreme asymmetries as assumed in Eq. (29) will typically not persist for larger T the linear dependence will be reduced for higher temperatures.

For low temperatures T , the spectrum A inside of the thermally activated energy interval will become symmetric with respect to ω , i.e., $A(k, \omega) \approx A(k)$. Then, the integral

$$I(\beta) = \int_{-\infty}^{\infty} d\omega \frac{\partial f(\omega, \beta)}{\partial \omega} \omega = 0$$

vanishes, since the integrand is an odd function. Thus for small $T \rightarrow 0$, the thermopower S is expected to converge to 0.

After these general considerations, we now return to $\text{Na}_{0.7}\text{CoO}_2$: In Fig. 13, we plot the imaginary part of the self-energies $\text{Im}\Sigma(i\omega)$ on the Matsubara axis and the k -integrated spectra $A(\omega)$ for various temperatures T . The high-energy tail of $\text{Im}\Sigma(i\omega)$ is determined by a sum rule,⁴⁶ and is therefore

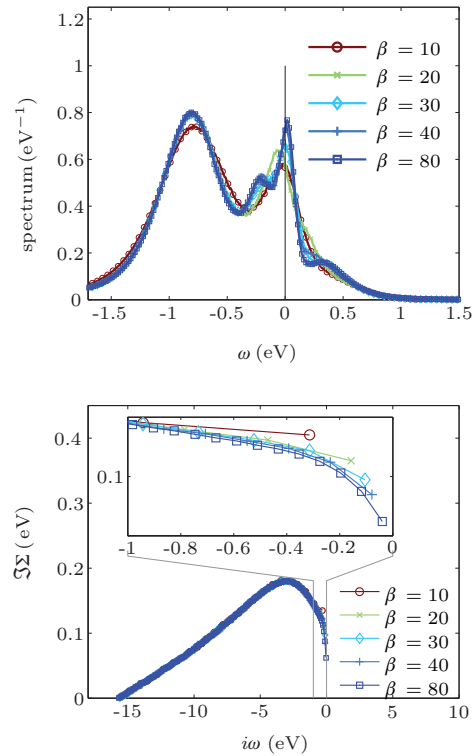


FIG. 13. (Color online) Top: k -integrated spectra $A(\omega)$ for various temperatures β in eV^{-1} . The spectral weight around the Fermi edge is decreasing with respect to temperature T . There is no major change of $\text{Im}\Sigma(i\omega)$ with respect to temperature, except for Matsubara frequencies ω_m close to the $\omega = 0$. Bottom: Self-energy $\text{Im}\Sigma(i\omega)$ on the Matsubara axis for various temperatures.

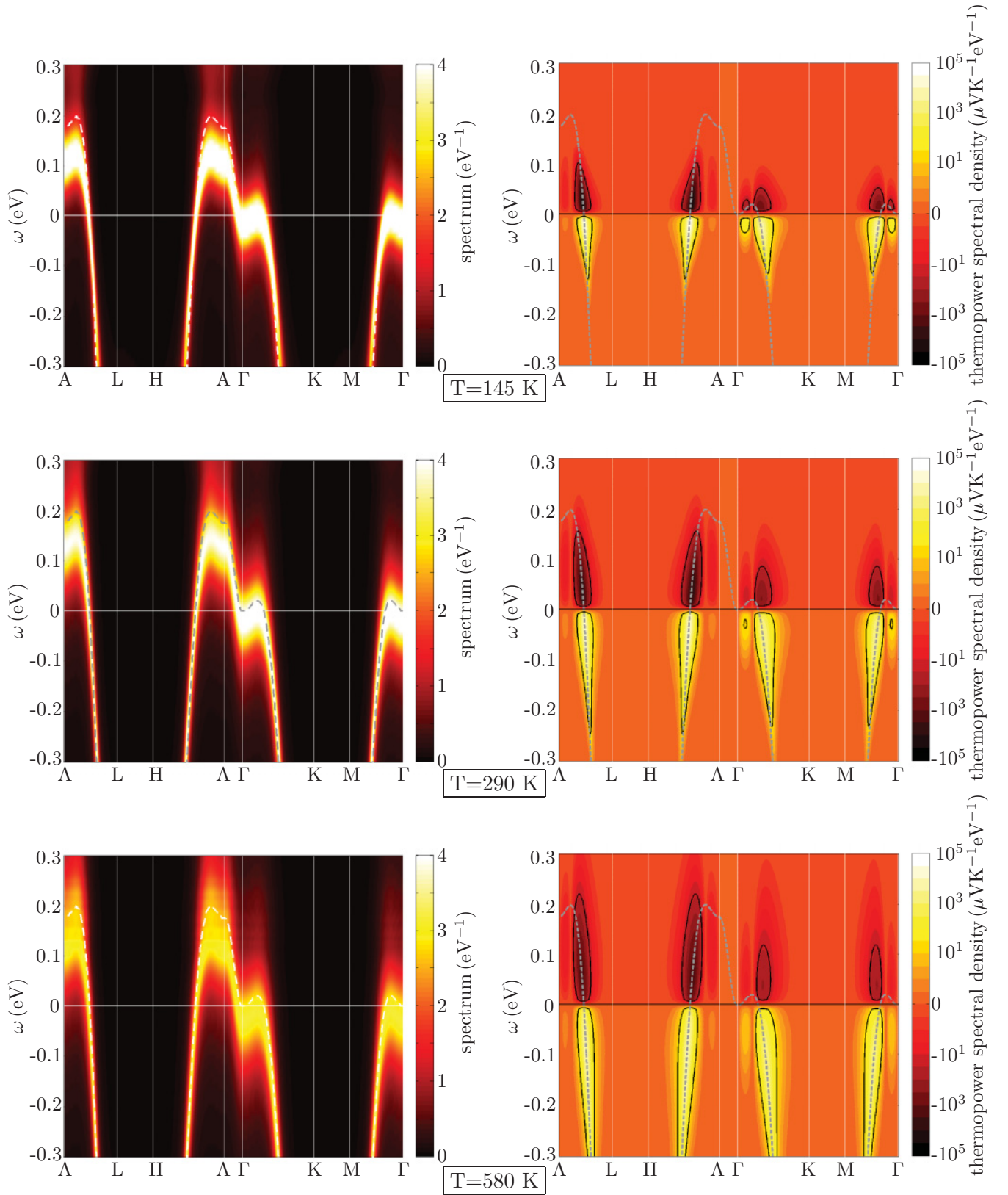


FIG. 14. (Color online) k -resolved spectra $A(k, \omega)$ (left) and corresponding thermopower spectral densities \mathcal{K}_{tot} (right) for various temperatures T . The color code is given by the color bar. The dashed line on the spectral images is the tight-binding fit. The spectral weight around the Fermi edge is decreasing with temperature. Thus the increase of the contribution to the thermopower gets dampened and is therefore not linear.

almost temperature independent. In the vicinity of $\omega = 0$, we observe a variation of $\text{Im}\Sigma(i\omega)$ with respect to temperature. This has several reasons: First, the highest Matsubara ω_m moves closer to $\omega = 0$ by definition and therefore we obtain a finer resolution. On the other hand, incoherent effects due to electron-electron scattering decrease with lower temperature.

The k -integrated spectrum plotted in Fig. 13 (top) shows less spectral weight of $A(\omega)$ in the vicinity of the Fermi edge for increasing temperature T . This is a usual effect of higher temperatures: the dampening of narrow peaks in the spectrum. In addition, there are no indications for a phase change to an insulator of the material in the investigated temperature interval 145–1160 K originated in the electronic structure, since the qualitative spectral distribution remains more or less unchanged. However, the result for $\beta = 20 \text{ eV}^{-1}$ is puzzling, because it shows a deviation of the general temperature behavior with respect to the other results. The same behavior is also observed for other doping $x_{\text{Na}} = 0.6, 0.8$. Most probably this result is connected to the numerical error in the employed maximum entropy method (MEM) as two spectral peaks merge into one.

In Fig. 14, we show how the k -resolved spectra and the thermopower spectral density \mathcal{K}_{tot} changes with temperature. We observe that the spectral weight is in fact decreasing in the thermally activated energy interval. Thus the linear approximation for $S(T)$ has to be adapted for the spectra of $\text{Na}_{0.7}\text{CoO}_2$. The linear increase will be dampened with increasing temperature leading to a flattening of $S(T)$. This can also be seen in the final results in Fig. 25, where we plot the thermopower $S(T)$ for various doping x_{Na} .

B. Effects of the disorder

Separating the effects of correlation and disorder is a highly nontrivial task. Generally, correlations seem to have a larger impact on the thermopower S than disorder in $\text{Na}_{0.7}\text{CoO}_2$. With the aim of understanding, we first set $U = 0 \text{ eV}$ and gradually increase the disorder potential $\Delta\varepsilon = 0 \rightarrow 1 \text{ eV}$. In the next section the opposite case, namely no disorder and increasing correlation, will be investigated.

The probability for a charge carrier to be scattered from one $\text{Co}_{\text{Na}} \leftrightarrow \text{Co}_{\text{vac}}$ site to the other is obviously proportional to the x_{Na} doping. On the other hand, the strength of the scattering event is determined by the disorder potential $\Delta\varepsilon$. In fact, $\Delta\varepsilon$ can be interpreted as an “electron affinity,” since a larger $\Delta\varepsilon$ will lead to more electrons occupying the Co_{Na} sites by means of the electrostatic attraction of the sodium ions.

In Sec. IV B, the importance of the self-energy $\Sigma(i\omega)$ on the imaginary axis has been discussed. With no correlation $U = 0$, we can observe the pure scattering effects of the disorder. In Fig. 15, the imaginary part of the self-energy $\text{Im}\Sigma(i\omega)$ is shown. The value $\lim_{\omega \rightarrow 0} \text{Im}\Sigma(i\omega)$ gradually increases as $\Delta\varepsilon = 0 \rightarrow 1 \text{ eV}$, which can be understood as follows: With the Green’s function $G := G(0)$ and the Weiss field $\mathcal{G}_0^{-1} := \mathcal{G}_0^{-1}(0)$, we make a CPA ansatz

$$G = \frac{x_{\text{Na}}}{\mathcal{G}_0^{-1} + \Delta\varepsilon} + \frac{1 - x_{\text{Na}}}{\mathcal{G}_0^{-1}}. \quad (30)$$

This means that the total (local) Green’s function consists of contributions corresponding to the sub lattice Co_{Na} and Co_{vac} ,

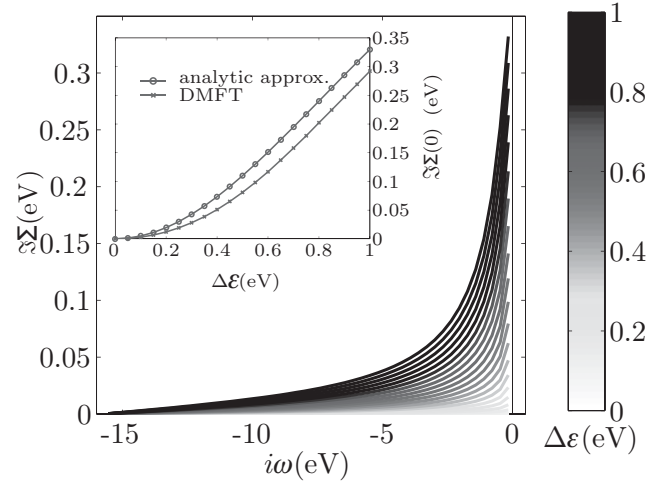


FIG. 15. (Color online) The imaginary part of the self-energy $\text{Im}\Sigma(i\omega)$ on the Matsubara axis for $T = 290 \text{ K}$ and $U = 0 \text{ eV}$ for various values of the disorder potential $\Delta\varepsilon = 0 \rightarrow 1 \text{ eV}$. A gradual increase of $\text{Im}\Sigma(i\omega)$ with respect to $\Delta\varepsilon$ is observed. Inset: The values $\lim_{\omega \rightarrow 0} \text{Im}\Sigma(i\omega)$ obtained by the approximate formula (34) and by DMFT. For small disorder $\Delta\varepsilon$ the approximation is in good agreement with the DMFT data.

where the former is energetically lowered by the disorder potential $\Delta\varepsilon$. As in the atomic limit, the task is to extract the self-energy $\Sigma = \Sigma(0)$ by expressing G of Eq. (30) with the corresponding Dyson equation

$$G = \frac{1}{\mathcal{G}_0^{-1} - \Sigma}. \quad (31)$$

After some algebra, we find

$$\Sigma = x_{\text{Na}} \Delta\varepsilon \frac{(1 - x_{\text{Na}}) \Delta\varepsilon \text{Re}\mathcal{G}_0 + i(1 - x_{\text{Na}}) \Delta\varepsilon \text{Im}\mathcal{G}_0}{[1 - (1 - x_{\text{Na}}) \Delta\varepsilon \text{Re}\mathcal{G}_0]^2 + [(1 - x_{\text{Na}}) \Delta\varepsilon \text{Im}\mathcal{G}_0]^2}. \quad (32)$$

To obtain an approximation of the Weiss field \mathcal{G}_0^{-1} , we use the Fourier transform of the noninteracting local Green’s function $G_0(\omega = 0)$,

$$\mathcal{G}_0 \approx \mathcal{P} \int d\varepsilon \frac{N(\varepsilon)}{-\varepsilon} + i\pi N(0), \quad (33)$$

where we used the Sokhotsky-Weierstrass theorem and $N(\varepsilon)$ denotes the noninteracting DOS. Note that we used the advanced version of the theorem, which means we will restrict to the part $\omega_m < 0$ of the self-energy $\Sigma(i\omega_m)$. Now, we assume a constant and symmetric DOS $N(\varepsilon) \approx N(0)\Theta(\varepsilon - \varepsilon_0)\Theta(\varepsilon_0 - \varepsilon)$ with $N(0) \approx 0.8 \text{ eV}^{-1}$ from Fig. 7. To that end, the principle value term drops in Eq. (33) and together with Eq. (32) we arrive at

$$\lim_{\omega \rightarrow 0} \text{Im}\Sigma(i\omega) \approx \frac{\pi x_{\text{Na}}(1 - x_{\text{Na}}) \Delta\varepsilon^2 N(0)}{1 + [\pi(1 - x_{\text{Na}}) \Delta\varepsilon N(0)]^2}. \quad (34)$$

The values of $\lim_{\omega \rightarrow 0} \text{Im}\Sigma(i\omega)$ as a function of $\Delta\varepsilon$ are plotted as an inset in Fig. 15, and compared to the self-consistently determined DMFT+CPA results. The DMFT+CPA data indicate quadratic dependence with respect to $\Delta\varepsilon$, which is properly approximated by our simple considerations.

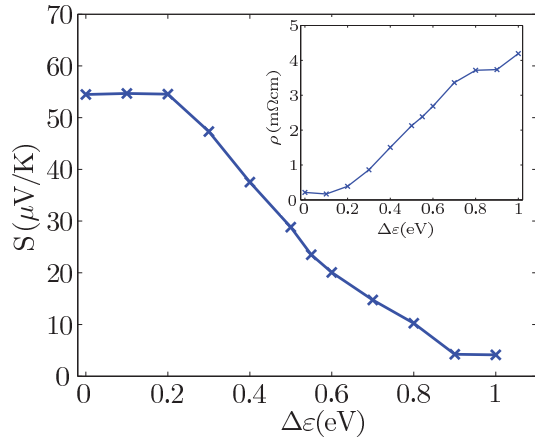


FIG. 16. (Color online) The thermopower S as a function of the disorder potential $\Delta\varepsilon$ without correlation ($U = 0$) for $T = 290$ K. The inset shows the corresponding values for the resistivity ρ . The magnitude of $S \sim K_1/K_0$ becomes smaller with larger $\Delta\varepsilon$, which can be traced back to a decrease of the current-heat correlation function K_1 dominating the increasing $\rho = 1/K_0$.

The approximate formula (34) indicates a direct connection between the disorder $\{x_{\text{Na}}, \Delta\varepsilon\}$ and the self-energy at low frequency, i.e. for $\lim_{\omega \rightarrow 0} \text{Im}\Sigma(i\omega)$. In fact, the value $\text{Im}\Sigma(0)$ can be interpreted as an inverse time τ_{dis}^{-1} , the average time which an electron spends at a site Co_{Na} or Co_{vac} , before scattering to the respective other site.

The increased scattering rate due to disorder is affecting both K_0 and K_1 . Numerical results indicate that K_1 is stronger suppressed than the conductivity K_0 which corresponds to an overall drastic decrease of the thermopower S , which is visualized in Fig. 16.

C. Effects of electronic correlation

After considering disorder without correlation in the previous section, we now focus on the effects of electron-electron correlation and assume that there is no disorder. At half filling $n/2 = 1/2$, it is well known that for increasing correlation U , a Mott metal-insulator transition can be observed (see, e.g., Ref. 13). This transition, which is entirely driven by electronic effects, is introduced in the following.

Away from half filling $n/2 < 1/2$, an electron occupying a certain site simply hops to a neighboring empty site without the necessity of a double occupancy (which would cost the energy U). Thus we additionally obtain standard conduction channels. An equivalent picture is also applicable for holes for $n/2 > 1/2$ as in our model material $\text{Na}_{0.7}\text{CoO}_2$. Without disorder, we have a mean filling of $n/2 = 0.85$, which is rather far away from $n/2 = 1/2$. For $U = 3.5$ eV, a renormalization of the noninteracting energy band of $Z = 0.77$ is obtained. Consequently, without disorder, electronic correlations are only intermediately strong. However, it pays to investigate the effect of correlation on the self-energy to compare with the case of combined disorder and correlation. In Fig. 17, we plot the imaginary part of the self-energy $\Sigma(i\omega)$ for different values of the correlation U . Several features can be observed: First, the maximum $\max\{\text{Im}\Sigma(i\omega)\} \sim U$. Second, the limit $\lim_{\omega \rightarrow 0} \text{Im}\Sigma(i\omega) \neq 0$ and the value depends on U .

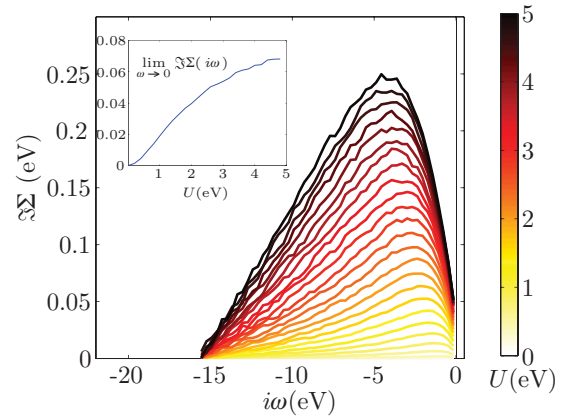


FIG. 17. (Color online) The imaginary part of the self-energy $\text{Im}\Sigma(i\omega)$ on the Matsubara axis for different values of the correlation $U = 0$ to 5 eV, and $T = 290$ K (no disorder). The actual values of U are according to the color bar on the right-hand side. Inset: The values of $\lim_{\omega \rightarrow 0} \text{Im}\Sigma(i\omega)$ as a function of U .

This behavior can be explained by means of Landau's Fermi-liquid theory, which predicts a dependence $\lim_{\omega \rightarrow 0} \text{Im}\Sigma(i\omega) \propto \alpha(U)T^2$. A visualization of the values $\lim_{\omega \rightarrow 0} \text{Im}\Sigma(i\omega)$ as a function of U can be found in the inset in Fig. 17.

In Fig. 18, we show the thermopower and the resistivity as a function of U with $\Delta\varepsilon = 0$. Larger U appears to increase ρ which reflects in the thermopower S . However, the change of S is much smaller than in the case of nonzero disorder $\Delta\varepsilon > 0$ below.

Correlation effects are small without the simultaneous consideration of disorder. When we include disorder, one of the two sites, namely Co_{vac} , will be driven closer to half filling.

D. Effects of combined disorder and correlation

The pure effects of disorder and correlation on self-energy and spectra were discussed in the previous two sections. Whether the observed characteristics of disorder and

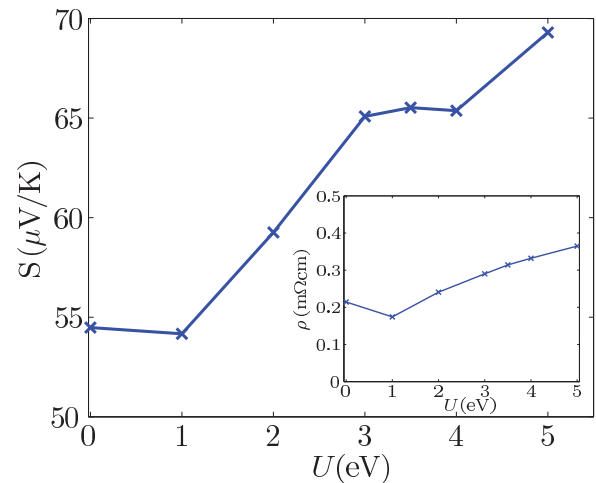


FIG. 18. (Color online) The thermopower S as a function of the correlation U without disorder ($\Delta\varepsilon = 0$) for $T = 290$ K. The inset shows the corresponding values for the resistivity ρ .

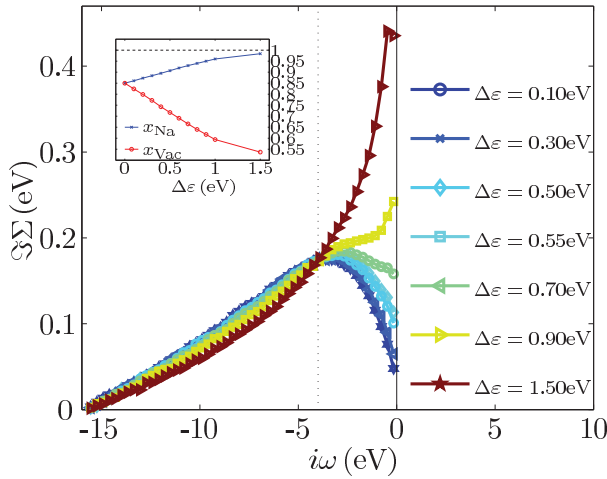


FIG. 19. (Color online) The imaginary part of the self-energy $\text{Im}\Sigma(i\omega)$ on the Matsubara axis for $T = 290$ K, $U = 3.5$ eV, and increasing values of the disorder potential $\Delta\varepsilon$. Inset: The filling per spin $n_{\text{Na}}, n_{\text{Vac}}$ at the two sites $\text{Co}_{\text{Na}}, \text{Co}_{\text{Vac}}$, respectively, as a function of the disorder potential $\Delta\varepsilon$.

correlation remain qualitatively unchanged in the presence of the other parameters, i.e., correlation or disorder, respectively, is yet to be investigated. We therefore fix either $U = 3.5$ eV or $\Delta\varepsilon = 0.55$ eV and vary the respective other parameter ($T = 290$ K and $x_{\text{Na}} = 0.7$).

In Fig. 19, the imaginary part of the self-energy $\text{Im}\Sigma(i\omega)$ for different values of the disorder potential $\Delta\varepsilon = 0 \rightarrow 1.5$ eV and fixed $U = 3.5$ eV is shown. Two main energy regions can be identified: In the high-energy region $\omega \lesssim -4$ eV the behavior of the self-energy is governed by the correlation U , which again can be explained by sum rules; cf. Ref. 46. On the other hand, between -4 and 0 eV, the slope of $\text{Im}\Sigma(i\omega)$ changes decisively with increasing $\Delta\varepsilon$. However, the latter part of the slope may again be explained by the arguments of Sec. IV B, since the values of $\lim_{\omega \rightarrow 0} \text{Im}\Sigma(i\omega)$ again depends approximately quadratically on the disorder $\Delta\varepsilon$ and agrees for small $\Delta\varepsilon$. For $\Delta\varepsilon = 1.5$ eV $\gtrsim t$, the system is already insulating, which is emphasized by an almost divergent $\text{Im}\Sigma$ in the vicinity of $\omega = 0$.

Another interesting numerical result is the filling of the a_{1g} orbital on the two sublattices Co_{Na} and Co_{Vac} as a function of $\Delta\varepsilon$, as visualized as an inset in Fig. 19. The filling n_{Na} rises in the analyzed $\Delta\varepsilon$ interval basically linearly to 1 as the disorder potential $\Delta\varepsilon$ increases, whereas n_{Vac} decreases. For very large disorder $\Delta\varepsilon = 1.5$ eV the fillings approach their maximum and minimal values $n_{\text{Na}}=1$ and $n_{\text{Vac}}=0.5$, respectively.

After the self-energy, we investigate the spectrum for increasing disorder potential $\Delta\varepsilon$. The k -integrated spectra $A(\omega)$ can be found in Fig. 20 (top). For $\Delta\varepsilon = 0 \rightarrow 1$ eV the spectral weight at the Fermi edge decreases, but the asymmetry of the spectral distribution with respect to $\omega = 0$ increases. A further increase $\Delta\varepsilon \gtrsim 1$ eV leads to the formation of a band gap and alloy band splitting created by disorder.

Though less spectral weight implies decreasing thermopower contributions for both electrons and holes [see \mathcal{K}_{tot} in Eq. (28) and Fig. 1], asymmetry in the spectrum with respect

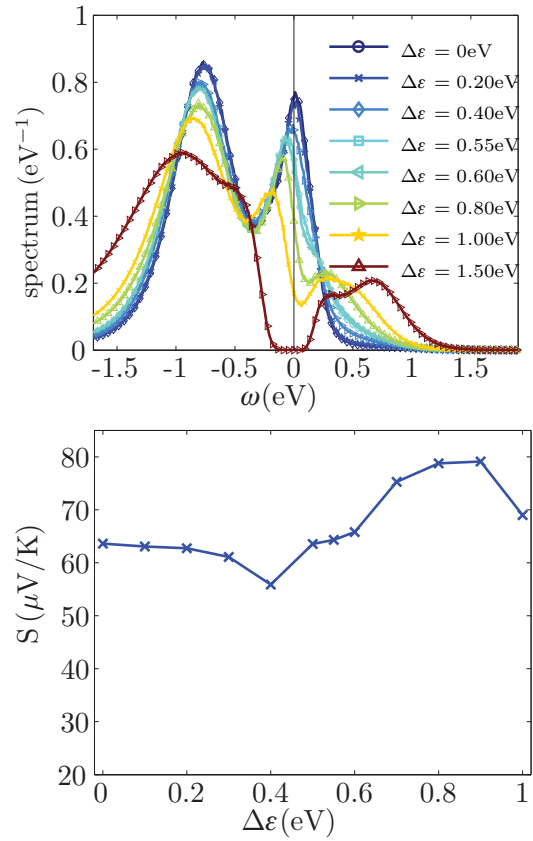


FIG. 20. (Color online) Top: k -integrated spectra for $U = 3.5$ eV, $T = 290$ K, and increasing disorder potential $\Delta\varepsilon$. Spectral weight at the Fermi edge $\omega = 0$ diminishes with increasing $\Delta\varepsilon$, but at the same time the asymmetry is increased. Bottom: The thermopower S as a function of the disorder potential $\Delta\varepsilon$ for a temperature $T = 290$ K. Starting from $S = 64$ $\mu\text{V}/\text{K}$ for $\Delta\varepsilon = 0$ eV the thermopower reaches a maximum $S = 79$ $\mu\text{V}/\text{K}$ for $\Delta\varepsilon = 0.9$ eV. For larger $\Delta\varepsilon > 0.9$ eV, a continuous decrease of S can be observed as the system becomes insulating.

to the Fermi edge $\omega = 0$ enhances S , and the thermopower thus nontrivially depends on the disorder. In Fig. 20 (bottom), we show the numerical results for the thermopower S as a function of the disorder potential $\Delta\varepsilon$. The slope shows a flat maximum of the thermopower $S = 80$ $\mu\text{V}/\text{K}$ for $\Delta\varepsilon \sim 0.7$ eV. For larger $\Delta\varepsilon \gtrsim 0.9$ eV, transport gets more and more suppressed as the spectral weight is shifted away from $\omega = 0$ and an alloy band gap forms. Again, the k -resolved spectra and contributions to the thermopower, shown in Fig. 23, enhance the understanding of these effects: For no disorder $\Delta\varepsilon = 0$ eV, we obtain a weak renormalization as discussed in Sec. V C. With a disorder of $\Delta\varepsilon = 0.7$ eV all the charge carriers get scattered, which can be seen in a more diffuse k -resolved spectrum [corresponding to a larger $\text{Im}\Sigma(i\omega_m)$]. However, as the corresponding contribution to the thermopower reveals, electrons become scattered stronger than holes. Therefore the net enhancement for the transport property S in Fig. 20 (bottom), can be explained by an increase of spectral weight for the holes $\omega < 0$ compared to the purely disordered model, which is larger than the, also observed, increase of spectral weight for electrons ($\omega > 0$). But for $\Delta\varepsilon > 0.8$ eV the

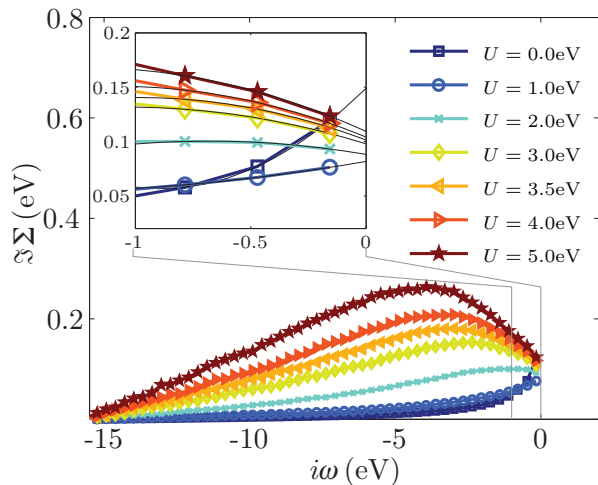


FIG. 21. (Color online) The imaginary part of the self-energy $\text{Im}\Sigma(i\omega)$ on the Matsubara axis for $T = 290$ K, $\Delta\varepsilon = 0.55$ eV, and increasing values of the correlation U . The black lines in the magnification are parabolic fits to the slopes. Note that the slopes converge to similar values for $\omega \rightarrow 0$, yet increase with larger U . For $U < \Delta\varepsilon$, the value of $\lim_{\omega \rightarrow 0} \text{Im}\Sigma(i\omega)$ appears to be governed by the disorder, while for larger U the shape of $\text{Im}\Sigma(i\omega)$ is mainly determined by correlation effects.

contribution of holes to the thermopower starts to diminish by a larger amount than can be accounted for by less negative contribution of the electrons. All charge carriers then are scattered at a high rate; the thermopower S consequently drops as the system becomes insulating.

After the numerical results for increasing disorder, we now fix $\Delta\varepsilon = 0.55$ eV and gradually increase the correlation $U = 0 \rightarrow 5$ eV. In Fig. 21, we plot the corresponding imaginary part $\text{Im}\Sigma(i\omega)$. Surprisingly, the value $\lim_{\omega \rightarrow 0} \text{Im}\Sigma(i\omega)$ first drops from 0.15 eV below 0.1 eV and then stabilizes around 0.1 eV for increasing correlation U . This indicates a rather nontrivial impact of a changing U on an already disordered system (the situation is further complicated since the Luttinger theorem does not hold due to disorder, and nonzero temperature, and the van Hove-like peak around the Fermi edge appears to react very sensitively to changes of U).

The effect of increasing correlation on the k -integrated spectrum is shown in Fig. 22 (top). A shift of spectral weight from just above to just below the Fermi level can be observed. This indicates an increase of the thermopower for larger U , which is indeed found as it is shown in Fig. 22 (bottom), where we show S function of U . The enhancement of $S = 25 \rightarrow 64$ $\mu\text{V}/\text{K}$ is extreme as $U = 0 \rightarrow 3$ eV. However, the growth of S gets saturated for $U \gtrsim 5$ eV.

To further improve our understanding, we again investigate the k -resolved spectra and corresponding contributions to the thermopower; cf. Fig. 24. Without correlation $U = 0$, there is little spectral weight directly around the Fermi edge. However, in that energy interval a larger U effectively packs spectral weight to a larger extent for holes than for electrons. Thus the drastic enhancement of S can be understood. For larger $U \sim 5$ eV, the change at the Fermi edge is not decisive, resulting in the saturation of the thermopower S with respect to U , shown in Fig. 22 (bottom).

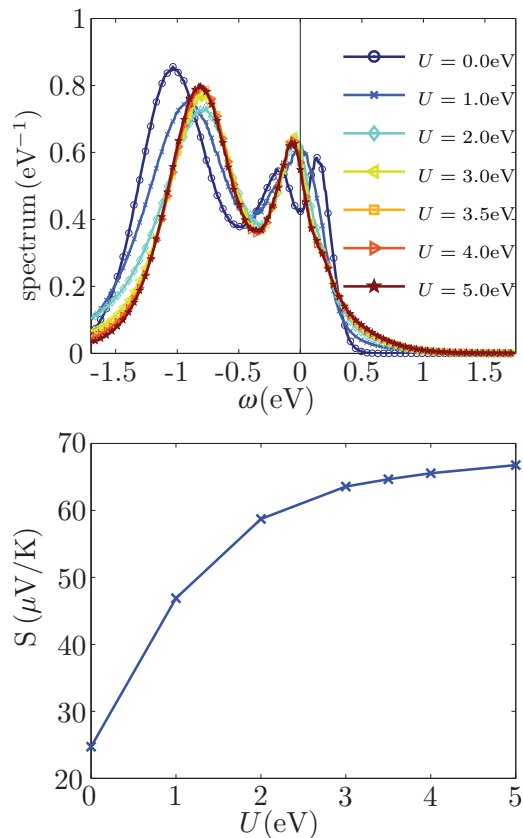


FIG. 22. (Color online) Top: k -integrated spectra for $\Delta\varepsilon = 0.55$ eV, $T = 290$ K, and increasing correlation U . Spectral weight is shifted from right above to right below the Fermi level $\omega = 0$. Bottom: Thermopower S as a function of the correlation U for a temperature $T = 290$ K. The thermopower increases from $S \approx 25$ $\mu\text{V}/\text{K}$ for $U = 0$ eV up to a maximal value of $S = 67$ $\mu\text{V}/\text{K}$ for $U \sim 4$ eV, where the effect is saturated.

E. Effects of the doping

The considerations of the previous sections are mostly thought experiments to identify the important effects in the model compound $\text{Na}_{0.7}\text{CoO}_2$. On the other hand, the typical external parameters that one can control in experiment are the temperature T and the doping x_{Na} . The gradual change or replacement of specific elements within a chemical compound has been used since ancient times. During the course of the 20th century, doping has become a major tool in technical applications and experimental materials science.

In semiconductor applications, one usually dopes by replacement: In addition to the main contents (e.g., Si), a similar element is added, which leaves the crystal structure in principle unchanged and takes the position of a fraction of the main chemical component(s). In the band structure, this procedure creates new bands that are energetically close to the ones of the desired charge carrier, and can therefore be much easier to thermally activate than in the pure compound.

In contrast to replacement, $\text{Na}_{0.7}\text{CoO}_2$ is doped by changing the sodium content; cf. Refs. 32–34. Since the single electron of the alkali Na becomes a valence electron in the cobaltate CoO_2 layers, this corresponds to shifting the Fermi energy

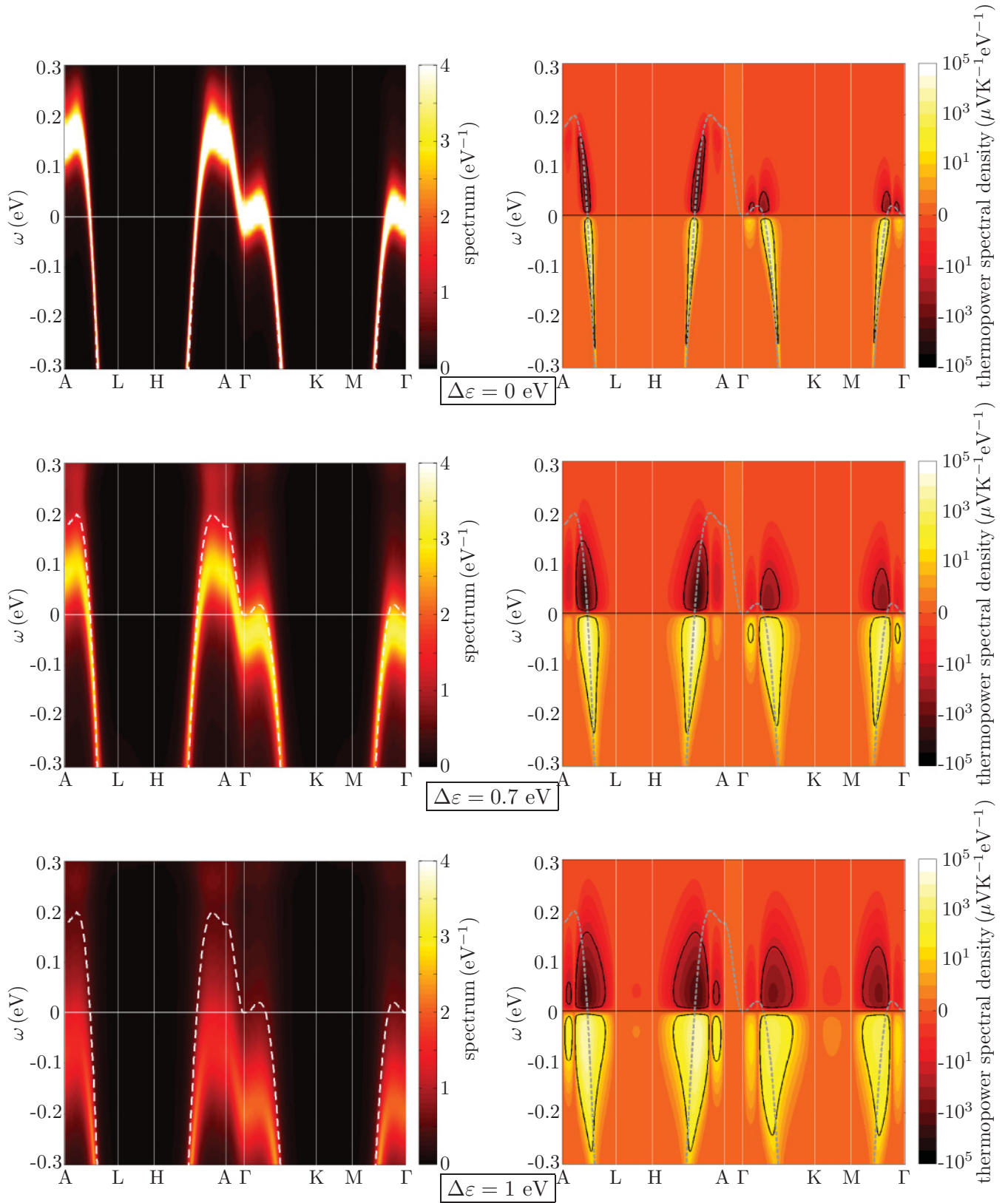


FIG. 23. (Color online) k -resolved spectra $A(k, \omega)$ (left) and corresponding thermopower spectral densities \mathcal{K}_{tot} (right) for various values for the disorder potential $\Delta\varepsilon = \{0 \text{ eV}, 0.7 \text{ eV}, 1 \text{ eV}\}$ at $T = 290 \text{ K}$. The color code is given by the color bar and the tight-binding fit is visualized as dashed line. The electronic contribution $\omega > 0$ to the thermopower is increased for $\Delta\varepsilon = 0.7 \text{ eV}$, but the hole contribution $\omega < 0$ is enhanced even more. For large values of $\Delta\varepsilon = 1 \text{ eV}$ spectral weight is diminishing above *and* below the Fermi edge.

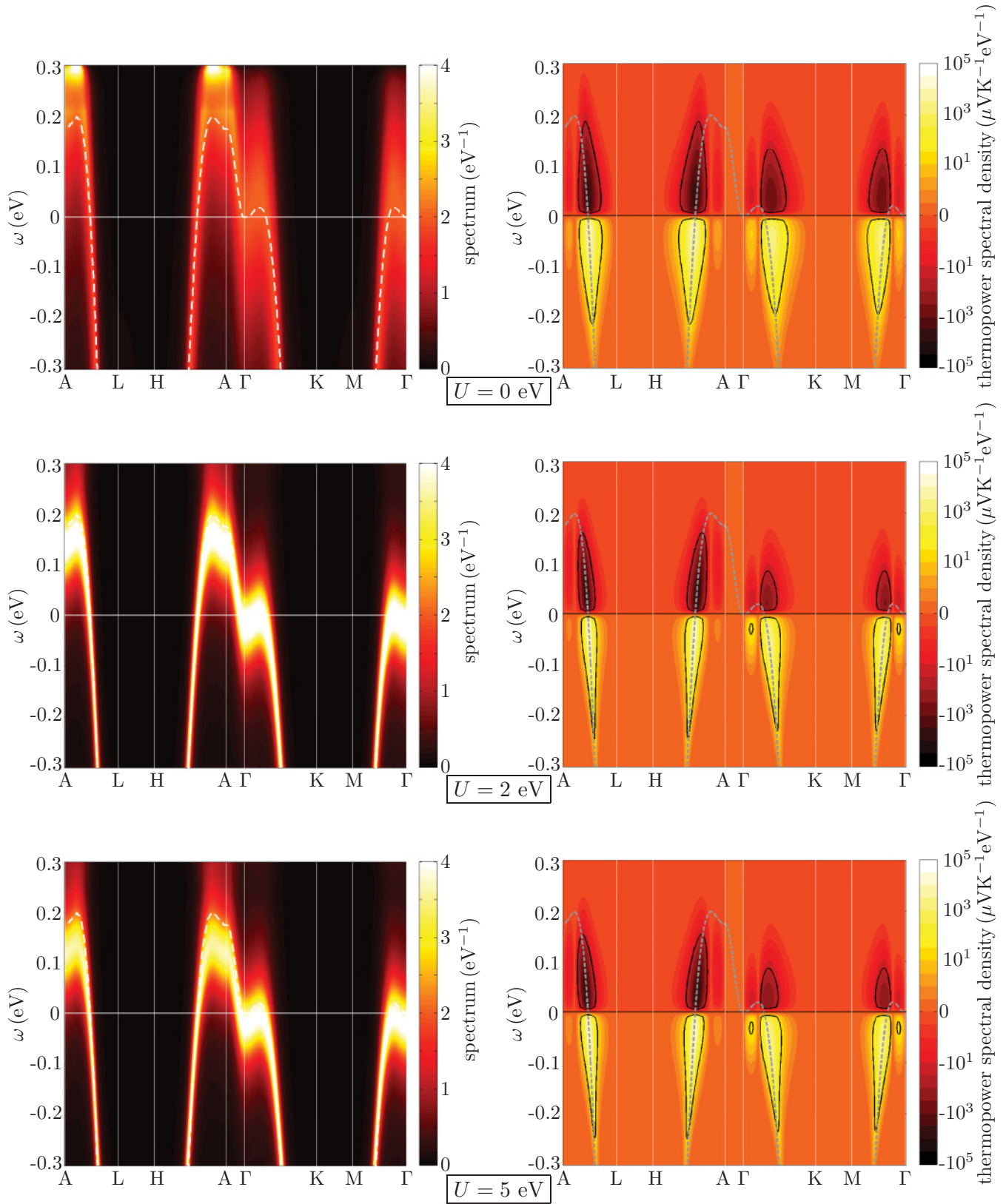


FIG. 24. (Color online) k -resolved spectra $A(k, \omega)$ (left) and corresponding thermopower spectral densities \mathcal{K}_{tot} (right) for various values for the correlation $U = \{0 \text{ eV}, 2 \text{ eV}, 5 \text{ eV}\}$ at $T = 290 \text{ K}$. The color code is given by the color bar and the tight-binding fit is shown as a dashed line. Spectral weight is shifted from above, directly below the Fermi edge $\omega = 0$ as $U = 0 \rightarrow 2 \text{ eV}$, which increases the hole contributions to S while decreasing the electron contribution. This effect is even stronger for $U = 5 \text{ eV}$.

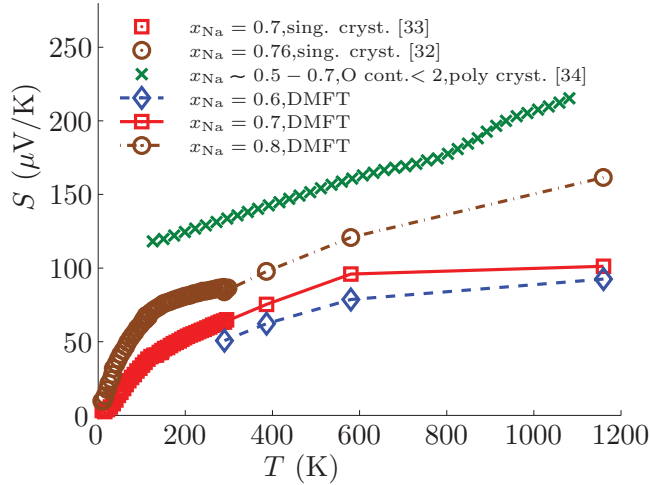


FIG. 25. (Color online) The thermopower S over the temperature T for $U = 3.5$ eV, $\Delta\varepsilon = 0.55$ eV, and various doping x_{Na} computed by DMFT compared to experiment. Transport in xy direction is assumed, $\tilde{v}_{xy}^2 = \tilde{v}_x^2 + \tilde{v}_y^2$. The thermopower increases nonlinearly with temperature T as discussed in Sec. IV A. For increasing doping x_{Na} , the thermopower increases for all temperatures T .

E_F within the a_{1g} band of the noninteracting band structure (Fig. 6).

As discussed in Sec. II and in Ref. 11, the pudding-mold-like slope of the a_{1g} band is expected to be a very important feature for a high thermopower S . The closer the Fermi energy E_F is to the flat top of the band, the larger the effect will be. Then, one charge carrier highly outmatches the other in terms of group velocity $\nabla\varepsilon(k)$. We therefore expect the thermopower to increase for higher x_{Na} . In fact, as can be seen in Fig. 25, the computations yield a larger thermopower S as the doping x_{Na} increases from $0.6 \rightarrow 0.8$. Here, we plot the thermopower S over temperature T for various doping x_{Na} and compare to experiment (see Ref. 9 for a corresponding comparison of the resistivity). The experimental results are in good agreement with our data, even though a direct comparison is made difficult, by the (in this case) unknown orientation of the crystal in the experiment. The result of larger thermopower S with increasing x_{Na} can be qualitatively explained by band-structure arguments. Still, there can be additional effects due to correlations and disorder. The k -integrated spectra in Fig. 26 indicate that spectral weight is shifted from electrons $\omega > 0$ to holes $\omega < 0$ as $x_{\text{Na}} = 0.6 \rightarrow 0.8$. This further enhances the pudding mold effect of the group velocity $\nabla\varepsilon$. The k -resolved spectra in Fig. 27 show another result: The pudding mold contribution of the k path in the xy plane $\Gamma \rightarrow K$ important for $x_{\text{Na}} = 0.6, 0.7$ is joined by the $k_z \neq 0$ contribution $A \rightarrow H$ as the Fermi level moves down. That provides an explanation why the dampening of the linear increase of the thermopower S becomes smaller as $x_{\text{Na}} = 0.7 \rightarrow 0.8$.

VI. CONCLUSION

In Na_xCoO_2 two distinct effects enhance the hole current in comparison to the electron one: a larger group velocity and a larger number of holes or, more precisely, a larger hole spectral weight,²⁴ also see Fig. 1. As both effects

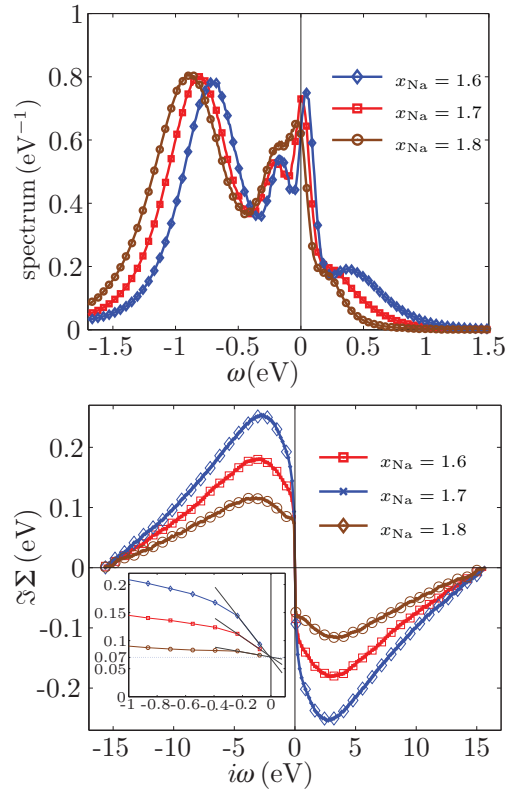


FIG. 26. (Color online) k -integrated spectra for $U = 3.5$ eV, $\Delta\varepsilon = 0.55$ eV, $T = 290$ K, and various doping x_{Na} . For $x_{\text{Na}} = 0.6$ the Fermi-liquid peak is the most pronounced as the filling of the site Co_{vac} is closest to $1/2$. In the vicinity of the Fermi edge, spectral weight is shifted from $\omega > 0$ to $\omega < 0$ as $x_{\text{Na}} = 0.6 \rightarrow 0.8$. Bottom: Imaginary part of the self-energy $\text{Im}\Sigma(i\omega)$ on the Matsubara axis for $U = 3.5$ eV, $\Delta\varepsilon = 0.55$ eV, $T = 290$ K, and various doping $x_{\text{Na}} = \{0.6, 0.7, 0.8\}$. Inset: Magnification around $\omega = 0$ and corresponding tangents (black). All slopes converge to similar values, which are independent of the disorder x_{Na} , but dependent on the disorder potential $\Delta\varepsilon$ and U .

point in the same direction, we obtain a large electron-hole imbalance. Consequently, a temperature gradient results in a higher hole current and hence a large positive thermopower S . The larger group velocity of the holes can be understood already from a one-particle LDA point of view. It is caused by the particular pudding-mold type of band-structure.¹¹ In this paper we analyzed the second mechanism, which is a genuine correlation effect. The microscopic origin is a complex interplay of Coulomb repulsion U and a (disordered) potential $\Delta\varepsilon$ due to the Na vacancies. We have hence taken U and $\Delta\varepsilon$ as free parameters (not *ab initio* ones as in Ref. 9). The Coulomb repulsion alone (without disorder) has only a rather minute impact. This is due to the filling of 1.7 electrons per Co site. With 0.3 holes in an otherwise filled Co a_{1g} orbital, chances to have two holes on the same Co site are very small. Hence the impact of the Coulomb repulsion, whose main effect is to suppress such configurations, is small. Without the vacancy potential, electronic correlations in Na_xCoO_2 would therefore be very weak. Without Coulomb repulsion, on the other hand, the vacancy disorder smears out the spectrum and particularly enhances the resistivity less than

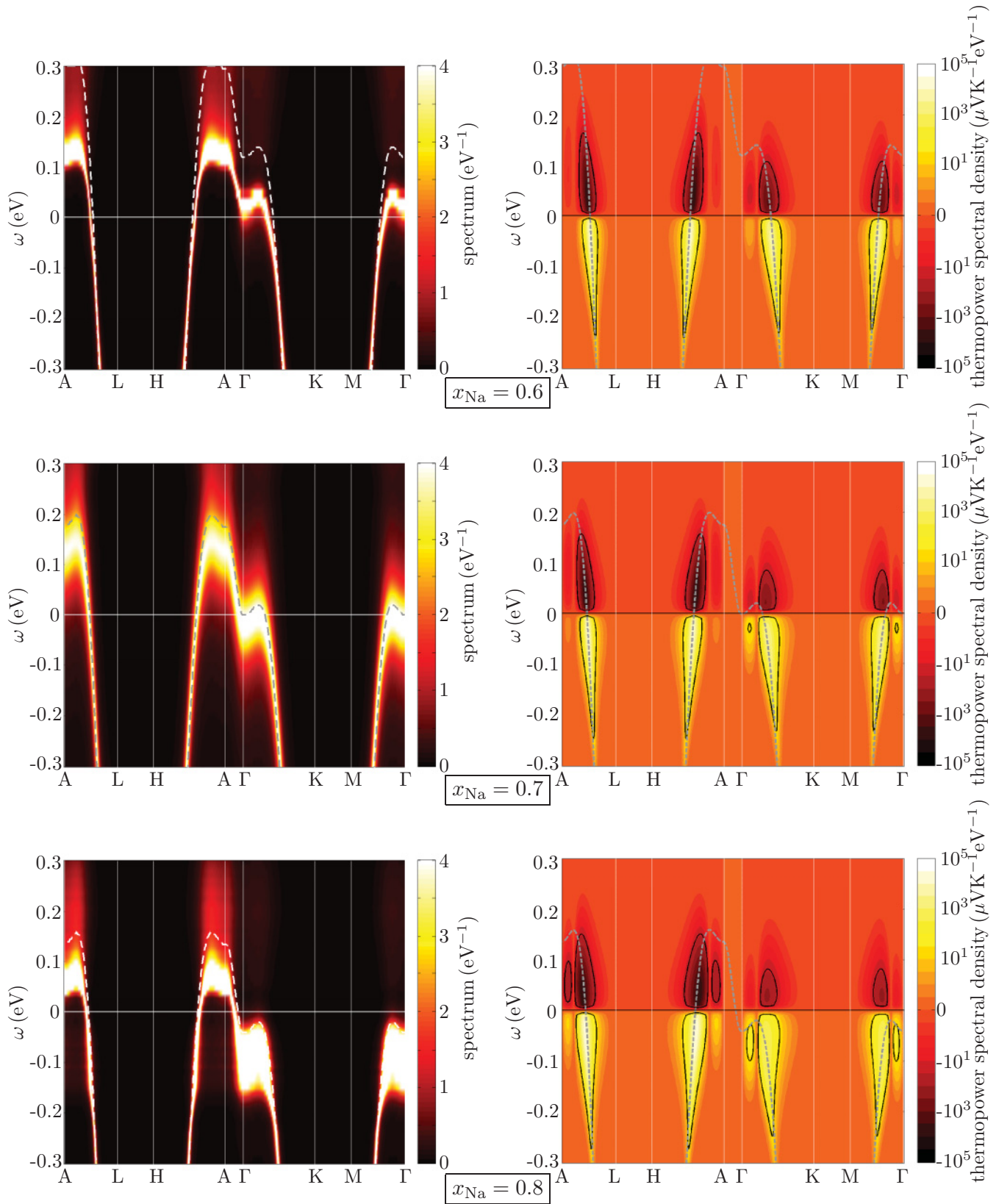


FIG. 27. (Color online) k -resolved spectra $A(k, \omega)$ (left) and corresponding thermopower spectral densities \mathcal{K}_{tot} (right) for $U = 3.5$ eV, $\Delta\varepsilon = 0.55$ eV, and various values of the doping x_{Na} . The color code is given by the color bar and the tight-binding fit is visualized by a dashed line. The (negative) electronic contribution to the thermopower is smaller as $x_{\text{Na}} = 0.6 \rightarrow 0.8$, thus the thermopower S shows a net increase. For $x_{\text{Na}} = 0.8$ also the pudding molds between $A \rightarrow H$ and $A \rightarrow L$ becomes important.

the current–heat-current correlation function is diminished, so that the thermopower actually decreases. The story becomes very different if Coulomb repulsion and disorder potential are combined. Then, the disorder potential gives rise to two inequivalent lattice sites. Since the number of holes in the a_{1g} exactly corresponds to the number of sites with a higher potential for the electrons, we end up with a situation close to two electrons on the Co sites with adjacent Na ion and one electron on the Co site with adjacent vacancy. In this situation, electronic correlations can be very strong for the half filled Co sites with an adjacent vacancy. Because of this, we get a strongly renormalized spectrum with a sharp peak at the Fermi level; see Fig. 9. The other sites, with adjacent Na ions, on the other hand, have only a sizable spectral weight on the hole side of the Fermi level. Taken together, we have more (quasi)holes but nonetheless sharp peaks in the spectrum. In this situation, the thermopower increases up to $80 \mu\text{V}/\text{K}$ with interaction. For a larger value of the disorder potential, the Coulomb interaction can even (counterintuitively) change the behavior from an insulator with a very small thermopower to a metal with a big one.

For tracing down the energy and momentum of the quasiparticles responsible for positive and negative thermopower alike, we have analyzed the various contributions to the thermopower separately. In Fig. 12, we show for which k and ω we have a significant contribution from the group velocity, the spectral weight, and for which interval holes and electrons can be thermally activated. We also introduced a thermoelectric spectral weight, which combines these terms and hence provides for a k - and ω -resolved analysis of the thermopower. The biggest

contributions naturally stem from those k vectors, which have the largest group velocity, albeit the quantitative contribution is changing in comparison to the noninteracting case. Most interestingly, also hole contributions appear that, without interaction, were not present at certain k points. Generally, electronic correlations change the energies and momenta with big contributions to the thermopower quite substantially.

As the vacancy (disorder) potential $\Delta\varepsilon$ is most crucial for the thermopower and the physical properties of Na_xCoO_2 in general, it is worthwhile to have a closer inspection of this parameter. Actually, in LDA calculations, $\Delta\varepsilon$ is rather small, i.e., ~ 0.05 eV (Ref. 10). This value is way too small to provide for the aforementioned charge disproportionation and the resulting strong electronic correlations on the Co sites with vacancy. Marianetti and Kotliar^{23,41} argued that LDA overestimates screening so that the actual $\Delta\varepsilon$ is much larger, i.e., ~ 0.55 eV. This is also the value we have considered in our paper as the physically relevant one. Besides the overestimation of screening, we think that the electron-phonon coupling is an important source for the effective increase of $\Delta\varepsilon$ by $\sim g^2/\omega_0$ (g : electron-phonon coupling strength; ω_0 : phonon frequency).

ACKNOWLEDGMENTS

We acknowledge the financial support from the FWF through GK W004 (P.W.), from the research unit FOR 1346 (A.T.), from the FWF through “Lise-Meitner” Grant No. M1136 (G.S.), and from the SFB ViCoM F41 (K.H.). Calculations have been done on the Vienna Scientific Cluster (VSC).

¹T. M. Tritt and M. A. Subramanian, *MRS Bull.* **31**, 188 (2006).

²M. Xie and D. M. Gruen, *J. Phys. Chem B* **114**, 14339 (2010).

³J. Fairbanks, in ECT 2008 – On line proceedings [available at ect2008.icmpe.cnrs.fr].

⁴J. P. Heremans *et al.*, *Science* **321**, 554 (2008).

⁵S. Paschen, in *CRC Handbook of Thermoelectrics*, edited by D. M. Rowe (CRC, Boca Raton, 2005), Chap. 15.

⁶J. K. Freericks, V. Zlatic, and A. M. Shvaika, *Phys. Rev. B* **75**, 035133 (2007).

⁷A. I. Hochbaum *et al.*, *Nature (London)* **451**, 163 (2008).

⁸A. I. Boukai *et al.*, *Nature (London)* **451**, 168 (2008).

⁹P. Wissgott, A. Toschi, H. Usui, K. Kuroki, and K. Held, *Phys. Rev. B* **82**, 201106(R) (2010).

¹⁰D. J. Singh, *Phys. Rev. B* **61**, 13397 (2000).

¹¹K. Kuroki and R. Arita, *J. Phys. Soc. Jpn.* **76**, 083707 (2007). Also note a related double pudding mold in LiRh_2O_4 ; R. Arita, K. Kuroki, K. Held, A. V. Lukoyanov, S. Skornyakov, and V. I. Anisimov, *Phys. Rev. B* **78**, 115121 (2008).

¹²W. Metzner and D. Vollhardt, *Phys. Rev. Lett.* **62**, 324 (1989).

¹³A. Georges and G. Kotliar, *Phys. Rev. B* **45**, 6479 (1992).

¹⁴A. Georges *et al.*, *Rev. Mod. Phys.* **68**, 13 (1996).

¹⁵V. I. Anisimov, A. I. Poteryaev, M. A. Korotin, A. O. Anokhin, and G. Kotliar, *J. Phys.: Condens. Matter* **9**, 7359 (1997).

¹⁶A. I. Lichtenstein and M. I. Katsnelson, *Phys. Rev. B* **57**, 6884 (1998).

¹⁷K. Held, *Adv. Phys.* **56**, 829 (2007).

¹⁸K. Held *et al.*, in *Properties and Applications of Thermoelectric Materials*, edited by V. Zlatic and A. Hewson (Springer, Dordrecht, 2009).

¹⁹Frank Lechermann, Silke Biermann, and Antoine Georges, *Prog. Theor. Phys. Suppl.* **160**, 233 (2005).

²⁰H. Ishida, M. D. Johannes, and A. Liebsch, *Phys. Rev. Lett.* **94**, 196401 (2005); A. Liebsch and H. Ishida, *Eur. Phys. J. B* **61**, 405 (2008).

²¹F. Lechermann, *Phys. Rev. Lett.* **102**, 046403 (2009).

²²C. A. Marianetti and G. Kotliar, *Phys. Rev. Lett.* **98**, 176405 (2007).

²³Also note exact diagonalization calculations for Hubbard and the t - J -model such as e.g. Jan O. Haerter, Michael R., R. Peterson and B. S. Shastry, *Phys. Rev. Lett.* **97**, 226402 (2006); B. S. Shastry, *Rep. Prog. Phys.* **72**, 016501 (2009).

²⁴More precisely, one should speak of quasielectrons and quasiholes.

²⁵J. Hubbard, *Proc. R. Soc. London, Ser. A* **276**, 238 (1963).

²⁶R. J. Elliott, J. A. Krumhansl, and P. L. Leath, *Rev. Mod. Phys.* **46**, 465–543 (1974).

²⁷R. Vlaming and D. Vollhardt, *Phys. Rev. B* **45**, 4637 (1992); J. Minár, L. Chioncel, A. Perlov, H. Ebert, M. I. Katsnelson, and A. I. Lichtenstein, *Phys. Rev. B* **72**, 045125 (2005).

²⁸G. D. Mahan, *Many-Particle Physics*, 2nd ed. Plenum, New York and London, 1990).

²⁹A. C. Durst and P. A. Lee, *Phys. Rev. B* **62**, 1270 (2000).

³⁰This intrinsic difference between conductance and thermopower is due to the fact that the electric field E distinguishes between

electrons and holes, whereas the temperature gradient ∇T , the driving force for thermopower, creates diffusion in the same direction of both electrons and holes.

- ³¹I. Terasaki, Y. Sasago, and K. Uchinokura, *Phys. Rev. B* **56**, R12685 (1997).
- ³²N. Kaurav, K. K. Wu, Y. K. Kuo, G. J. Shu, and F. C. Chou, *Phys. Rev. B* **79**, 075105 (2009).
- ³³M. Lee *et al.*, *Nat. Mater.* **5**, 537 (2006).
- ³⁴H. Yakabe *et al.*, in *Thermoelectrics, Proceedings ICT 98. XVII International Conference* (Nagoya, Japan, 1998), pp. 551-558.
- ³⁵R. E. Schaak *et al.*, *Nature (London)* **424**, 527 (2003).
- ³⁶K. Sugira *et al.*, *Inorg. Chem.* **45**, 1894 (2006).
- ³⁷R. J. Balsys and R. L. Davis, *Solid State Ionics* **93**, 279 (1997).
- ³⁸Q. Huang, B. Khaykovich, F. C. Chou, J. H. Cho, J. W. Lynn, and Y. S. Lee, *Phys. Rev. B* **70**, 134115 (2004).
- ³⁹H. W. Zandbergen, M. L. Foo, Q. Xu, V. Kumar, and R. J. Cava, *Phys. Rev. B* **70**, 024101 (2004).
- ⁴⁰Some experiments (Ref. 37) indicate the migration of the Na ions, and, at lower temperatures, the Na ions might also form a superstructure; see Ref. 39.
- ⁴¹The strength of the disorder potential $\Delta\varepsilon$ is very sensitive to screening effects and thus depends on the localization of the t_{2g} electrons (Ref. 23). In the LDA calculation, where screening is overestimated, $\Delta\varepsilon$ is much smaller than 0.55 eV. However, correlation effects may lead to an even larger $\Delta\varepsilon$. The value $\Delta\varepsilon = 0.55$ from Ref. 23 is thus an intermediate choice between these two extremes. In a real *ab initio* approach, one would have to determine the disorder potential $\Delta\varepsilon$ self-consistently (i.e., including correlations).
- ⁴²The Fourier transforms needed for the DMFT cycle have been performed using the Ulmke smoothing scheme, which implies that $\text{Im}(\Sigma)$ shown here artificially vanishes at the Nyquist frequency; see M. Ulmke, V. Janis, and D. Vollhardt, *Phys. Rev. B* **51**, 10411 (1995).
- ⁴³J. Skilling, *Fundamental Theories of Physics* (Dordrecht, Kluwer, Cambridge, England, 1989), Vol. 36.
- ⁴⁴M. Jarrel *et al.*, *Lectures on the Physics of Strongly Correlated Systems XII*, AIP Conference Proceedings No. 1014, edited by A. Avella and F. Mancini (AIP, Melville NY, 2007).
- ⁴⁵H.-B. Yang *et al.*, *Phys. Rev. Lett.* **92**, 246403 (2004).
- ⁴⁶Y. Vilc and A.-M. Tremblay, *J. Phys. I (France)* **7**, 1309 (1997).